Biomech Model Mechanobiol (2016) 15:43–67
DOI 10.1007/s10237-015-0705-x

ORIGINAL PAPER

A multiscale mechanobiological model of bone remodelling predicts site-specific bone loss in the femur during osteoporosis and mechanical disuse

C. Lerebours[1] · P. R. Buenzli[1] · S. Scheiner[2] · P. Pivonka[3]

Received: 27 February 2015 / Accepted: 5 July 2015 / Published online: 4 August 2015

Abstract We propose a multiscale mechanobiological model of bone remodelling to investigate the site-specific evolution of bone volume fraction across the midshaft of a femur. The model includes hormonal regulation and biochemical coupling of bone cell populations, the influence of the microstructure on bone turnover rate, and mechanical adaptation of the tissue. Both microscopic and tissue-scale stress/strain states of the tissue are calculated from macroscopic loads by a combination of beam theory and micromechanical homogenisation. This model is applied to simulate the spatio-temporal evolution of a human midshaft femur scan subjected to two deregulating circumstances: (i) osteoporosis and (ii) mechanical disuse. Both simulated deregulations led to endocortical bone loss, cortical wall thinning and expansion of the medullary cavity, in accordance with experimental findings. Our model suggests that these observations are attributable to a large extent to the influence of the microstructure on bone turnover rate. Mechanical adaptation is found to help preserve intracortical bone matrix near the periosteum. Moreover, it leads to non-uniform cortical wall thickness due to the asymmetry of macroscopic loads introduced by the bending moment. The effect of mechanical adaptation near the endosteum can be greatly affected by whether the mechanical stimulus includes stress concentration effects or not.

✉ C. Lerebours
chloe.lerebours@monash.edu

[1] School of Mathematical Sciences, Monash University, Clayton, VIC 3800, Australia

[2] Institute for Mechanics of Materials and Structures, TU Wien, Vienna University of Technology, Karlsplatz 13/202, 1040 Vienna, Austria

[3] St Vincent's Department of Surgery, The University of Melbourne, Fitzroy, VIC 3065, Australia

Keywords Bone remodelling · Site-specific bone loss · Trabecularisation · Multiscale modelling · Osteoporosis · Mechanical disuse

1 Introduction

Bone is a biomaterial with a complex hierarchical structure characterised by at least three distinct length scales: (i) the cellular scale (10–20 μm); (ii) the tissue scale (2–5 mm); and (iii) the whole organ scale (4–45 cm) (Rho et al. 1998; Weiner and Wagner 1998). Several interactions exist between these scales, which affect bone remodelling, bone material properties and bone structural integrity. The activity of bone-resorbing and bone-forming cells during bone remodelling leads to changes in material properties at the tissue scale which subsequently affect the distribution of loads at the structural, whole organ scale (Fig. 1). Besides, changes in bone shape and microarchitecture modify the stress/strain distribution and bone surface availability, which provide mechanical and geometrical feedbacks onto the bone cells and, eventually, affect bone remodelling (Martin 1972; Lanyon et al. 1982; Frost 1987). Due to the complexity of these interactions, the interpretation of experimental data at a single scale is difficult. Predicting the evolution of multifactorial bone disorders, such as osteoporosis, necessitates a comprehensive modelling approach in which these multiscale interactions are consistently integrated.

Various mathematical models of bone remodelling have been proposed in the literature. Biomechanics models estimating tissue-scale stress and strain distributions from musculoskeletal models and average material properties, such as bone density, are often used in conjunction with remodelling algorithms based on Wolff's law. These remodelling algorithms locally increase or decrease bone density depend-

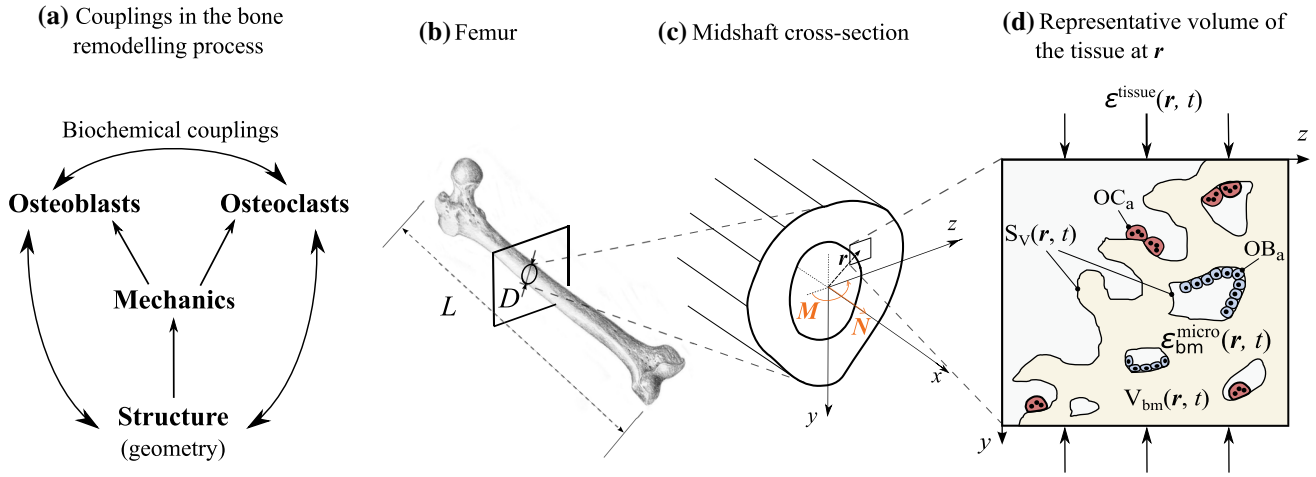

Fig. 1 Multiscale representation of bone. **a** Scheme of the couplings in the bone remodelling process; **b** femur bone geometry (organ scale); **c** midshaft cross section depicting coordinate axes and the sectional forces used for beam theory (tissue to organ scales); **d** representative volume element (RVE) of cortical bone used to define bone cell densities, bone volume fraction and specific surface (cellular to tissue scales)

ing on the tissue's mechanical state (Carter and Hayes 1977; Carter and Beaupré 2001; Fyhrie and Carter 1986; Weinans et al. 1992; Van der Meulen et al. 1993; Pettermann et al. 1997). Such models may also include damage accumulation due to fatigue loading and damage repair (Prendergast and Taylor 1994; McNamara and Prendergast 2007; García-Aznar et al. 2005). Other models focus at the microstructural scale (μm to mm) and describe the evolution of trabecular bone microarchitecture through resorption and formation events at the bone surface induced by the local mechanical state (Huiskes et al. 2000; Ruimerman et al. 2005; Van Oers et al. 2008; Christen et al. 2012, 2013). Most of these mathematical models focus on the biomechanical aspects of bone remodelling and do not consider hormonal regulation or biochemical coupling between bone cells.

In this paper, we propose a novel multiscale modelling approach of bone remodelling combining and extending several mathematical models into a consistent framework. This framework enables (i) the consideration of biochemical and cellular interactions in bone remodelling at the cellular scale (Lemaire et al. 2004; Pivonka et al. 2008; Buenzli et al. 2012; Pivonka et al. 2013), (ii) the evolution of material properties at the tissue scale based on bone cell remodelling activities regulated by mechanical feedback (Scheiner et al. 2013) and bone surface availability (Pivonka et al. 2013; Buenzli et al. 2013), and (iii) the determination of the stress/ strain distributions from the tissue scale to the microstructural scale by a combination of generalised beam theory and micromechanical homogenisation (Hellmich et al. 2008; Scheiner et al. 2013; Buenzli et al. 2013).

This modelling approach is applied to simulate the temporal evolution of a human femoral bone at the midshaft (Fig. 1), subjected to various deregulating circumstances such as osteoporosis and changes in mechanical loading. An initial state of normal bone remodelling is first assumed, in which the tissue across the midshaft cross section remodels at site-specific turnover rates without changing its average material properties. Osteoporosis is then simulated by hormonal changes deregulating the biochemical coupling between osteoclasts and osteoblasts. These hormonal changes are calibrated so as to reproduce realistic rates of osteoporotic bone loss. The strength of the resorptive and formative responses of bone cells to mechanical feedback is calibrated so as to reproduce rates of bone loss and recovery in cosmonauts undertaking long-duration space flight missions. A scan of a femur cross section is used as initial condition for our simulations. This illustrates the potential of our modelling approach to be used as a predictive, patient-specific diagnostic tool for estimating the deterioration of bone tissues. Here, we use the model to investigate the interplay between geometrical and mechanical feedbacks in inducing site-specific bone loss in osteoporosis, which is characterised by endocortical bone loss, cortical wall thinning and the expansion of the marrow cavity (Feik et al. 1997; Bousson et al. 2001; Zebaze et al. 2010).

2 Description of the model

Figures 1 and 2 summarise the general approach of our model. We consider a portion of human femur near the midshaft. This portion of bone is assumed to carry loads corresponding to a total normal force $\boldsymbol{N}$ and total bending moment $\boldsymbol{M}$ (Fig. 1c). These loads are distributed unevenly across the midshaft cross section depending on the site-specific bone microstructure, particularly on the cortical porosity (Zebaze et al. 2010; Buenzli et al. 2013). This load distribution determines a site-specific mechanical stimulus

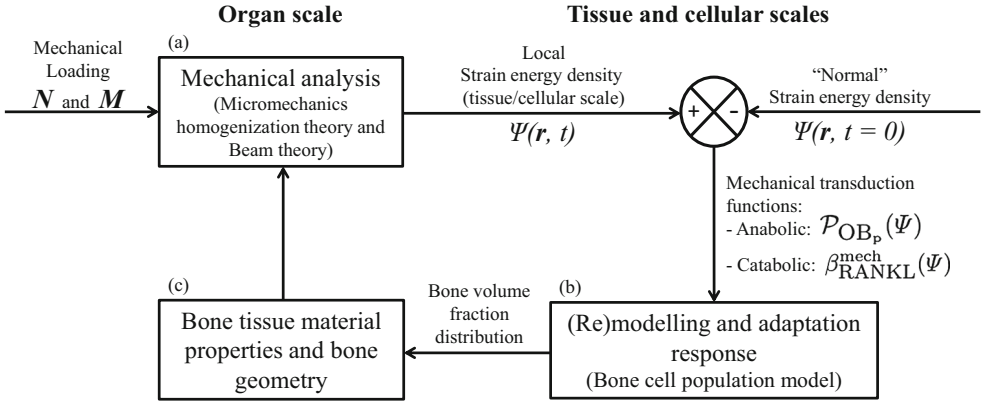

Fig. 2 Flow chart of bone remodelling simulations taking into account (*a*) the global mechanical loading, (*b*) the bone cell population model and (*c*) the bone material and geometry adaptation

which is sensed and transduced by bone cells (Fig. 2a). This mechanical feedback is incorporated in a cell population model as biochemical signals leading to changes in the balance between osteoclasts and osteoblasts (Fig. 2b). In addition, microstructural parameters such as bone volume fraction (f_{bm}) and bone specific surface influence the propensity of bone cells to differentiate and become active (Martin 1984; Lerebours et al. 2015). This geometrical feedback is included in the cell population model via a dependence of the bone turnover rate on the bone volume fraction. The activities of osteoclasts and osteoblasts modify the tissue microstructural parameters (bone volume fraction, bone specific surface), which in turn induce changes in the load distribution (Fig. 2c). In the following, we introduce in more detail the multiple scales and related variables involved in this model workflow. Table 1, in the section "Model parameter values" of the Appendix, lists all the parameters of the model.

2.1 Load distribution from the organ scale to the cellular scale

Loading is composed of body weight and muscle forces exerted onto bone via tendons and direct action of muscles. These forces can be calculated from bone shape, muscle and tendon attachment, and gait analysis data using musculoskeletal models (Lloyd and Besier 2003; Viceconti et al. 2006; Martelli et al. 2014). Continuum mechanics provides the link between external forces exerted onto a structure, and the strain and stress distribution in the structure (Salencon 2001).

Tissue-scale properties within the framework of continuum mechanics are average mechanical properties over microstructural material phases and pores (presented in detail in the next sections). The corresponding tissue-scale stresses and strains may significantly deviate from the microscopic, cellular scale, stresses and strains acting in the different material phases composing the tissue due to so-called strain and stress concentration effects (Zaoui 2002; Hill 1963). Microscopic stress and strain distributions in the bone matrix are likely to be sensed directly by bone cells, particularly by osteocytes (Scheiner et al. 2013). However, as osteocytes form an extensive interconnected network (Marotti 2000; Buenzli and Sims 2015), they may also sense larger scale stress and strain distributions. We will let either the tissue-scale or the microscopic mechanical state of bone act onto the bone cells to investigate how this influences the site-specific evolution of bone tissue microstructures.

In the following, we present first how stress and strain distributions can be calculated at the tissue scale using beam theory. We then present how these tissue-scale stress and strain distributions are employed as site-specific loading boundary conditions to the continuum micromechanical model of Hellmich et al. (2008) for the calculation of microscopic stress and strain distributions effective at the cellular level.

2.1.1 Determination of tissue-scale stress and strain distributions based on beam theory

The continuum mechanical field equations allow the calculation of tissue-scale strain and stress distributions in bone. Given that the length of the femur L is significantly larger (45–50 cm) than its diameter D (3–5 cm) at the midshaft (Fig. 1b), the continuum mechanical field equations can be approximated using beam theory formulated for small strains and generalised to materials of non-uniform properties, an approach we have used previously in Buenzli et al. (2013).

This approach requires the knowledge of the total external forces, i.e. the normal force $\boldsymbol{N}$ and the bending moment $\boldsymbol{M}$ carried by the femur cross section. $\boldsymbol{N}$ and $\boldsymbol{M}$ can be estimated for different physical activities by using musculoskeletal models (Vaughan et al. 1992; Forner-Cordero et al.

2006). In our simulations, we take constant values for $\boldsymbol{N}$ and $\boldsymbol{M}$ comparable with the maximum ground reaction force and knee and hip moments that occur during a gait analysis, estimated as: $\boldsymbol{N} = (N_x, 0, 0)$, $N_x = -700$N, and $\boldsymbol{M} = M\,\hat{\boldsymbol{m}}$, $M = 50$Nm, where $\hat{\boldsymbol{m}}$ is a unit vector along the antero-posterior axis of the cross section determined from the microradiograph (Vaughan et al. 1992; Forner-Cordero et al. 2006; Ruff 2000; Cordey and Gautier 1999) (Fig. 6c). The x-axis is the femur's longitudinal axis, and (y,z) is the plane transverse to x at the midshaft (Fig. 1b, c).

Tissue-scale mechanical properties correspond to spatial averages over a so-called representative volume element (RVE) of the tissue. In cortical bone, an appropriate tissue RVE is of the order of $10 \times 2 \times 2\,\text{mm}^3$, a size large enough to contain a large number of pores, but small enough to retain site-specific information and to not be influenced by macroscopic features such as overall bone shape (Hill 1963; Zaoui 2002). We denote by $\mathbb{C}^{\text{tissue}}(\boldsymbol{r}, t)$ the local bone tissue stiffness tensor defined at the RVE scale, where $\boldsymbol{r}$ denotes the location in bone of the RVE (Fig. 1c), and the dependence on time t reflects the fact that bone remodelling may modify the local mechanical properties of the tissue. This tissue-scale stiffness tensor is assumed to relate the tissue-scale stress tensor $\boldsymbol{\sigma}^{\text{tissue}}$ and strain tensor $\boldsymbol{\varepsilon}^{\text{tissue}}$ pointwise according to Hooke's law:

$$\boldsymbol{\sigma}^{\text{tissue}}(\boldsymbol{r}, t) = \mathbb{C}^{\text{tissue}}(\boldsymbol{r}, t) : \boldsymbol{\varepsilon}^{\text{tissue}}(\boldsymbol{r}, t). \tag{1}$$

Beam theory is based on the so-called Euler–Bernoulli kinematic hypothesis, which asserts that material cross sections initially normal to the beam's neutral axis remain planar, undeformed in their own plane, and normal to the neutral axis in the beam's deformed state (Timoshenko and Goodier 1951; Bauchau and Craig 2009; Hjelmstad 2005). These assumptions are expected to be well satisfied near the femoral midshaft under small deformations generated by bending and compression or tension. Furthermore, no shear force, torsional loads or twisting along the beam axis are assumed. These assumptions, Eq. (1), and the fact that bone is an orthotropic material (Hellmich et al. 2004) imply that the only nonzero components of the stress tensor are the normal stresses $\sigma_{xx}^{\text{tissue}} = \mathbb{C}_{1111}^{\text{tissue}}\varepsilon_{xx}^{\text{tissue}}$, $\sigma_{yy}^{\text{tissue}} = \mathbb{C}_{1122}^{\text{tissue}}\varepsilon_{xx}^{\text{tissue}}$ and $\sigma_{zz}^{\text{tissue}} = \mathbb{C}_{1133}^{\text{tissue}}\varepsilon_{xx}^{\text{tissue}}$, where the normal stresses $\sigma_{yy}^{\text{tissue}}$ and $\sigma_{zz}^{\text{tissue}}$ are induced by compression or tension along the beam axis x by the Poisson effect[1] (see Buenzli et al. 2013 for more details). The Euler–Bernoulli hypothesis implies that the tissue strain tensor reduces to the single nonzero component $\varepsilon_{xx}^{\text{tissue}}$ and that:

$$\varepsilon_{xx}^{\text{tissue}}(y, z, t) = \varepsilon_1(t) - \kappa_3(t)y + \kappa_2(t)z, \tag{2}$$

where ε_1 is the sectional axial strain, and κ_2 and κ_3 are the sectional beam curvatures about the z- and y-axes, respectively (Bauchau and Craig 2009). The three unknowns ε_1, κ_2 and κ_3 are determined by the constraints that (i) the integral of $\sigma_{xx}^{\text{tissue}}$ over the midshaft cross section must give the total normal force N_x, and (ii) the integral of the stress moment $(0, y, z) \times \sigma_{xx}^{\text{tissue}}\hat{\boldsymbol{x}}$ must give the total bending moment $\boldsymbol{M} = M\,\hat{\boldsymbol{m}}$ [the axes origin in the (y, z) plane is set at the modulus-weighted centroid of the section, also called normal force centre (Bauchau and Craig 2009)]. Explicit formulas for ε_1, κ_2 and κ_3 as functions of $\mathbb{C}^{\text{tissue}}$, $\boldsymbol{N}$ and $\boldsymbol{M}$ are presented in the section "Generalised Beam theory for inhomogeneous materials" of the Appendix. We refer the reader to Bauchau and Craig (2009), Sect. 6.3 and Buenzli et al. (2013) for their derivation.

2.1.2 *Determination of microscopic stress and strain distributions based on micromechanical homogenisation theory*

Bone tissue stiffness $\mathbb{C}^{\text{tissue}}$ is strongly influenced by the tissue's microstructure, in particular its porosity, or equivalently, its bone volume fraction f_{bm}. Bone volume fraction is a microstructural parameter defined at the tissue scale as the volume fraction of bone matrix in the RVE (Fig. 1d): $f_{\text{bm}} = \text{BV/TV} = 1 - \text{porosity}$, where BV is the volume of bone matrix in the RVE and TV is the tissue volume, i.e. the total volume of the RVE (Dempster et al. 2013). In Buenzli et al. (2013), we used an explicit power-law relationship $\mathbb{C}_{1111}^{\text{tissue}}(f_{\text{bm}}) \propto {f_{\text{bm}}}^3$ based on experimental relationships between bone stiffness and bone mineral content (Carter and Hayes 1977; Hernandez et al. 2001). While regression approaches based on power-law relations are able to account for material properties in one principal direction, they are less accurate in estimating material properties in other principal directions.

Here, we follow a different approach taken by Hellmich and colleagues using the framework of continuum micromechanics (Hill 1963, 1965; Zaoui 1997, 2002; Hellmich et al. 2004, 2008; Fritsch and Hellmich 2007; Fritsch et al. 2009). Mechanically, bone tissue can be considered as a two-phase material: a bone matrix phase ('bm') consisting of mineralised bone matrix, and a vascular phase ('vas') consisting of vascular components, cells, extracellular matrix and other soft tissues present in Haversian canals and in the marrow.

Continuum micromechanics provides a framework to estimate the tissue-scale stiffness tensor $\mathbb{C}^{\text{tissue}}(f_{\text{bm}})$ from the microscopic stiffness properties of bone matrix and vascular pores, and considerations regarding pore microarchitecture and phase interactions (Hellmich et al. 2008). The advantage

[1] The stress components $\sigma_{yy}^{\text{tissue}}$ and $\sigma_{zz}^{\text{tissue}}$ do not participate directly to the transfer of the resultant force $\boldsymbol{N}$ and resultant bending moment $\boldsymbol{M}$ across the bone cross section; however, they are accounted for in the calculation of the tissue-scale strain energy density Ψ^{tissue}.

of this approach is to provide (i) accurate three-dimensional estimates of $\mathbb{C}^{\text{tissue}}$ and (ii) estimates of the microscopic stress and strain distributions of the bone matrix without recourse to costly microfinite element analyses of the tissue microstructure (Fritsch et al. 2009). Using the concept of continuum micromechanics is justified in bone due to the separation of length scales between the RVE size and the characteristic sizes of the two-phase microstructures (Hellmich et al. 2008; Scheiner et al. 2013). We summarise below the premises upon which this approach is based.

The tissue-scale stress and strain tensors $\boldsymbol{\sigma}^{\text{tissue}}$ and $\boldsymbol{\varepsilon}^{\text{tissue}}$ correspond to spatial averages over the RVE of the microscopic (cellular-scale) stress and strain tensors. Assuming that each phase within the RVE is homogeneous, these spatial averages can be expressed as sums over the phases:

$$\boldsymbol{\sigma}^{\text{tissue}}(\boldsymbol{r},t) \equiv \frac{1}{\text{TV}}\int_{\text{TV}} \boldsymbol{\sigma}^{\text{micro}}\mathrm{d}V = \sum_k f_k\,\boldsymbol{\sigma}_k^{\text{micro}}, \tag{3}$$

$$\boldsymbol{\varepsilon}^{\text{tissue}}(\boldsymbol{r},t) \equiv \frac{1}{\text{TV}}\int_{\text{TV}} \boldsymbol{\varepsilon}^{\text{micro}}\mathrm{d}V = \sum_k f_k\,\boldsymbol{\varepsilon}_k^{\text{micro}}, \tag{4}$$

where $f_k(\boldsymbol{r},t)$ is the volume fraction of phase k ('bm', 'vas'), $\boldsymbol{\sigma}_k^{\text{micro}}(\boldsymbol{r},t)$ and $\boldsymbol{\varepsilon}_k^{\text{micro}}(\boldsymbol{r},t)$ are the microscopic stress and strain tensors in phase k. We emphasise that all these quantities still depend on the tissue-scale location $\boldsymbol{r}$ of the RVE in bone, while microscopic inhomogeneities are encoded in the phase index k. It can be shown that due to the linearity of the constitutive equations, the phase strain tensor $\boldsymbol{\varepsilon}_k^{\text{micro}}$ is related linearly with the tissue-scale strain tensor:

$$\boldsymbol{\varepsilon}_k^{\text{micro}} = \mathbb{A}_k : \boldsymbol{\varepsilon}^{\text{tissue}}, \tag{5}$$

where $\mathbb{A}_k$ is a fourth-order tensor called the strain concentration tensor (Zaoui 2002; Hellmich et al. 2008; Fritsch et al. 2009). Assuming that Hooke's law also holds for each phase at the microscopic scale, $\boldsymbol{\sigma}_k^{\text{micro}} = \mathbb{c}_k^{\text{micro}} : \boldsymbol{\varepsilon}_k^{\text{micro}}$ (with $\mathbb{c}_k^{\text{micro}}$ the stiffness tensor of phase k), one obtains from Eqs. (3) and (5):

$$\begin{aligned}\boldsymbol{\sigma}^{\text{tissue}} &= \sum_k f_k\,\mathbb{c}_k^{\text{micro}} : \boldsymbol{\varepsilon}_k^{\text{micro}} \\ &= \left(\sum_k f_k\,\mathbb{c}_k^{\text{micro}} : \mathbb{A}_k\right) : \boldsymbol{\varepsilon}^{\text{tissue}} \equiv \mathbb{C}^{\text{tissue}} : \boldsymbol{\varepsilon}^{\text{tissue}},\end{aligned} \tag{6}$$

where

$$\mathbb{C}^{\text{tissue}} = f_{\text{bm}}\,\mathbb{c}_{\text{bm}}^{\text{micro}} : \mathbb{A}_{\text{bm}} + f_{\text{vas}}\,\mathbb{c}_{\text{vas}}^{\text{micro}} : \mathbb{A}_{\text{vas}}. \tag{7}$$

Equation (7) provides a relationship between the tissue-scale stiffness, $\mathbb{C}^{\text{tissue}}$, and the microscopic properties of the phases composing the tissue, $f_k, \mathbb{c}_k^{\text{micro}}$ and $\mathbb{A}_k$. Because mineral content across bone tissues only varies little on average (Scheiner et al. 2013; Fritsch and Hellmich 2007), $\mathbb{c}_{\text{bm}}^{\text{micro}}$ can be assumed constant and homogeneous, i.e. independent of $\boldsymbol{r}, t$. The elastic modulus $\mathbb{c}_{\text{vas}}^{\text{micro}}$ is likewise assumed independent of $\boldsymbol{r}, t$ and taken as that of water (Scheiner et al. 2013). Both $\mathbb{c}_{\text{bm}}^{\text{micro}}$ and $\mathbb{c}_{\text{vas}}^{\text{micro}}$ have been measured experimentally, and their values are listed in Table 1. The strain concentration tensors $\mathbb{A}_k$ can be estimated by solving so-called matrix-inclusion problems of elasticity homogenisation theory, which use assumptions on phase shape within the RVE and phase interactions (Eshelby 1957; Laws 1977). For bone, accurate multi-scale homogenisation schemes were developed and validated experimentally (Hellmich et al. 2008; Fritsch et al. 2009; Morin and Hellmich 2014). These schemes provide explicit expressions for $\mathbb{A}_k$ depending on the phase volume fractions f_{bm} and f_{vas}. Because $f_{\text{vas}} = 1 - f_{\text{bm}}$, this defines both the f_{bm} dependence of $\mathbb{C}^{\text{tissue}}$ via Eq. (7), and a method to estimate the strains and stresses in the bone matrix at the microscopic level from those known at the tissue level:

$$\boldsymbol{\varepsilon}_{\text{bm}}^{\text{micro}}(\boldsymbol{r},t) = \mathbb{A}_{\text{bm}}(f_{\text{bm}}) : \boldsymbol{\varepsilon}^{\text{tissue}} \tag{8}$$

$$\begin{aligned}\boldsymbol{\sigma}_{\text{bm}}^{\text{micro}}(\boldsymbol{r},t) &= \mathbb{c}_{\text{bm}}^{\text{micro}} : \left(\mathbb{A}_{\text{bm}}(f_{\text{bm}}) : \boldsymbol{\varepsilon}^{\text{tissue}}\right) \\ &\equiv \mathbb{B}_{\text{bm}}(f_{\text{bm}}) : \boldsymbol{\sigma}^{\text{tissue}},\end{aligned} \tag{9}$$

where Hooke's law, Eq. (1), was used in the last equality in Eq. (9). The stiffness tensor $\mathbb{C}^{\text{tissue}}(f_{\text{bm}})$, the strain concentration tensor $\mathbb{A}_{\text{bm}}(f_{\text{bm}})$ and the stress concentration tensor $\mathbb{B}_{\text{bm}}(f_{\text{bm}})$ can be evaluated numerically at each location $\boldsymbol{r}$ in the femur midshaft cross section and each time t based on the value of $f_{\text{bm}}(\boldsymbol{r},t)$ and the expressions given in Fritsch and Hellmich (2007) and Scheiner et al. (2013).

Combined with beam theory, this procedure enables us to completely determine, at each time t, the spatial distribution across the femur midshaft of (i) the tissue-scale stress and strain tensors, $\boldsymbol{\sigma}^{\text{tissue}}$, $\boldsymbol{\varepsilon}^{\text{tissue}}$; and (ii) the microscopic stress and strain tensors of bone matrix, $\boldsymbol{\sigma}_{\text{bm}}^{\text{micro}}$, $\boldsymbol{\varepsilon}_{\text{bm}}^{\text{micro}}$.

In this paper, we will consider both the tissue-scale strain energy density (SED), Ψ^{tissue}, and microscopic SED of the bone matrix, $\Psi_{\text{bm}}^{\text{micro}}$, as local mechanical quantities sensed and transduced by bone cells. These SEDs are defined by:

$$\Psi^{\text{tissue}}(\boldsymbol{r},t) = \tfrac{1}{2}\boldsymbol{\varepsilon}^{\text{tissue}} : \mathbb{C}^{\text{tissue}} : \boldsymbol{\varepsilon}^{\text{tissue}}, \tag{10}$$

$$\Psi_{\text{bm}}^{\text{micro}}(\boldsymbol{r},t) = \tfrac{1}{2}\boldsymbol{\varepsilon}_{\text{bm}}^{\text{micro}} : \mathbb{c}_{\text{bm}}^{\text{micro}} : \boldsymbol{\varepsilon}_{\text{bm}}^{\text{micro}}. \tag{11}$$

The SEDs defined in Eqs. (10) and (11) will be used to formulate biomechanical regulation in the bone remodelling equations. In the literature, biomechanical regulation is commonly based on the SED since this quantity is scalar and it integrates both microstructural state and loading environment (Fyhrie and Carter 1986; Mullender et al. 1994; Ruimerman et al. 2005).

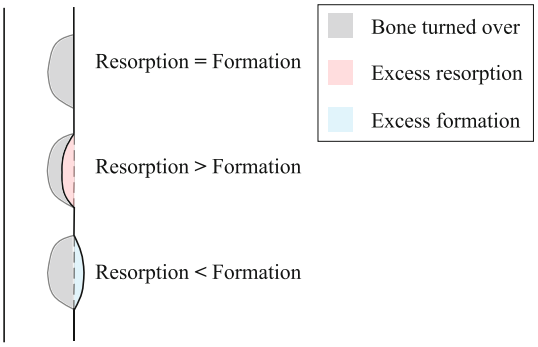

Fig. 3 Schematic representation of the definition of bone turnover provided by Eq. (13) in cases of balanced remodelling, remodelling with bone loss and remodelling with bone gain

2.2 Bone tissue remodelling

The tissue is assumed to be remodelled by a population of active osteoclasts ($\mathrm{OC_a}$) and active osteoblasts ($\mathrm{OB_a}$). Active osteoclasts are assumed to resorb bone at rate k_{res} (volume of bone resorbed per cell per unit time). Active osteoblasts are assumed to secrete new bone matrix at rate k_{form} (volume of bone formed per cell per unit time). These cellular resorption and formation rates are taken to be constant and uniform. However, the bone volume fraction $f_{\mathrm{bm}}(\boldsymbol{r},t)$ of the tissue may evolve with site-specific rates depending on the balance between the populations of active osteoclasts and active osteoblasts (Martin 1972; Buenzli et al. 2013):

$$\frac{\partial}{\partial t} f_{\mathrm{bm}}(\boldsymbol{r},t) = k_{\mathrm{form}}\mathrm{OB_a} - k_{\mathrm{res}}\mathrm{OC_a}. \tag{12}$$

In Eq. (12), $\mathrm{OC_a}(\boldsymbol{r},t)$ and $\mathrm{OB_a}(\boldsymbol{r},t)$ denote the average densities of active osteoclasts and active osteoblasts in the tissue located at $\boldsymbol{r}$ (number of cells in the RVE/TV, Fig. 1d). The site-specific remodelling rate $\chi_{\mathrm{BV}}(\boldsymbol{r},t)$ of the tissue at $\boldsymbol{r}$ (also called turnover rate) can be defined as the volume fraction of bone in the RVE that is resorbed and refilled in matched amount per unit time. This corresponds to the minimum of the volume fraction of bone resorbed per unit time, $k_{\mathrm{res}}\mathrm{OC_a}$, and volume fraction of bone formed per unit time, $k_{\mathrm{form}}\mathrm{OB_a}$ (Parfitt 1983, Sect. II.C.2.c.ii):

$$\chi_{\mathrm{BV}}(\boldsymbol{r},t) = \min\{k_{\mathrm{res}}\mathrm{OC_a}, k_{\mathrm{form}}\mathrm{OB_a}\}. \tag{13}$$

Any imbalance between resorption and formation in Eq. (12) corresponds to surplus resorption or surplus formation with respect to the baseline of bone properly turned over in Eq. (13), as shown in Fig. 3.

Equation (12) enables us to track site-specific modifications of the midshaft tissue microstructure through $f_{\mathrm{bm}}(\boldsymbol{r},t)$, from which stress and strain distributions across the midshaft can be estimated at both the tissue scale and the microscopic, cellular scale, by means of Eqs. (34)–(35) and (8)–(11).

2.3 Bone cell population model

It remains to specify how the populations of active osteoclasts $\mathrm{OC_a}(\boldsymbol{r},t)$ and active osteoblasts $\mathrm{OB_a}(\boldsymbol{r},t)$ evolve in the RVE located at $\boldsymbol{r}$ under mechanobiological, geometrical and biochemical regulations. For this, we use a continuum cell population model based on rate equations, originally developed by Lemaire et al. (2004), and later refined and extended by Pivonka and co-workers (Pivonka et al. 2008, 2010; Buenzli et al. 2012; Pivonka et al. 2013; Scheiner et al. 2013; Pivonka et al. 2012).

To highlight important biochemical couplings and regulations in osteoclastogenesis and osteoblastogenesis, several differentiation stages of osteoclasts and osteoblasts are considered. These biochemical interactions are mediated by several signalling molecules whose binding kinetics are explicitly considered in the model, such as transforming growth factor β (TGFβ), receptor activator of nuclear factor κB (RANK) and associated ligand RANKL, osteoprotegerin (OPG) and parathyroid hormone (PTH). The biochemical network of these couplings and regulations is summarised in Fig. 4.

Active osteoclasts ($\mathrm{OC_a}$s) denote cells attached to the bone surface that actively resorb bone matrix. These cells are assumed to differentiate from a pool of osteoclast precursor cells ($\mathrm{OC_p}$s) by the binding of RANKL to the RANK receptor, expressed on $\mathrm{OC_p}$s, which induces intracellular NFκB signalling. Osteoclast precursors are assumed to differentiate from a pool of uncommitted osteoclasts progenitors ($\mathrm{OC_u}$), such as haematopoietic stem cells, under the action of macrophage colony stimulating factor (MCSF) and RANKL signalling (Roodman 1999; Martin 2004).

Active osteoblasts ($\mathrm{OB_a}$s) denote cells at the bone surface that actively deposit new bone matrix. These cells are assumed to differentiate from a pool of osteoblast precursor cells ($\mathrm{OB_p}$s). This activation is inhibited in the presence of TGFβ. Osteoblast precursors are assumed to differentiate from a pool of uncommitted osteoblasts progenitors ($\mathrm{OB_u}$), such as mesenchymal stem cells or bone marrow stromal cells, upon TGFβ signalling (Roodman 1999).

The rate equations governing the evolution of the tissue-average cell densities are given by:

$$\begin{aligned}\frac{\partial}{\partial t}\mathrm{OC_p}(\boldsymbol{r},t) &= \mathcal{D}_{\mathrm{OC_u}}\big(\mathrm{MCSF},\,\mathrm{RANKL}(\Psi,\mathrm{PTH})\big)\,\mathrm{OC_u}(f_{\mathrm{bm}}) \\ &\quad - \mathcal{D}_{\mathrm{OC_p}}\big(\mathrm{RANKL}(\Psi,\mathrm{PTH})\big)\,\mathrm{OC_p}, \end{aligned}\tag{14}$$

$$\begin{aligned}\frac{\partial}{\partial t}\mathrm{OC_a}(\boldsymbol{r},t) &= \mathcal{D}_{\mathrm{OC_p}}\big(\mathrm{RANKL}(\Psi,\mathrm{PTH})\big)\,\mathrm{OC_p} \\ &\quad - \mathcal{A}_{\mathrm{OC_a}}(\mathrm{TGF\beta})\,\mathrm{OC_a}, \end{aligned}\tag{15}$$

$$\begin{aligned}\frac{\partial}{\partial t}\mathrm{OB_p}(\boldsymbol{r},t) &= \mathcal{D}_{\mathrm{OB_u}}(\mathrm{TGF\beta})\,\mathrm{OB_u}(f_{\mathrm{bm}}) + \mathcal{P}_{\mathrm{OB_p}}(\Psi)\,\mathrm{OB_p} \\ &\quad - \mathcal{D}_{\mathrm{OB_p}}(\mathrm{TGF\beta})\,\mathrm{OB_p}, \end{aligned}\tag{16}$$

$$\begin{aligned}\frac{\partial}{\partial t}\mathrm{OB_a}(\boldsymbol{r},t) &= \mathcal{D}_{\mathrm{OB_p}}(\mathrm{TGF\beta})\,\mathrm{OB_p} \\ &\quad - A_{\mathrm{OB_a}}\mathrm{OB_a}, \end{aligned}\tag{17}$$

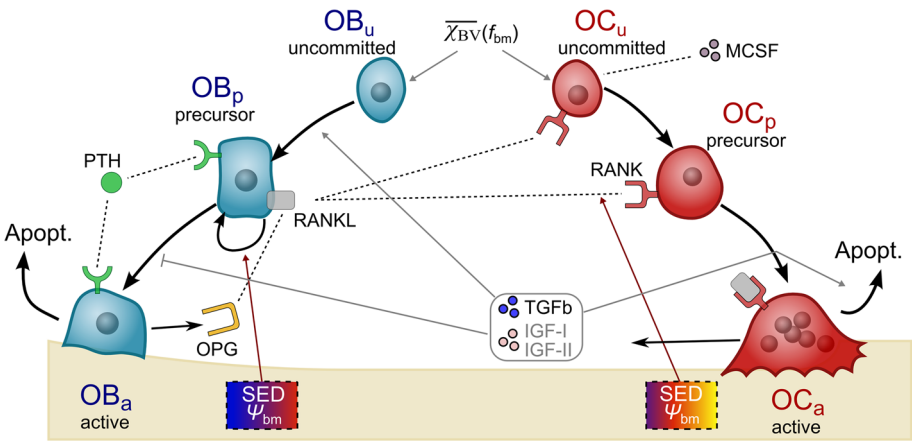

Fig. 4 Proposed cell population model of bone remodelling taking into account several developmental stages of osteoblasts and osteoclasts together with biochemical regulation, biomechanical regulation (via strain energy density, Ψ) and geometrical regulation (via the turnover function, $\overline{\chi_{\mathrm{BV}}}(f_{\mathrm{bm}})$)

where $\mathcal{D}_i$ is the differentiation rate of cell type i ($i = \mathrm{OC_u}, \mathrm{OC_p}, \mathrm{OB_u}, \mathrm{OB_p}$) modulated by signalling molecules, $\mathcal{A}_{\mathrm{OC_a}}$ is the apoptosis rate of active osteoclasts modulated by TGFβ, $A_{\mathrm{OB_a}}$ is the (constant) apoptosis rate of active osteoblasts, $\mathcal{P}_{\mathrm{OB_p}}$ is the proliferation rate of osteoblast precursor cells and Ψ is the strain energy density, taken to be either Ψ^{tissue} or $\Psi_{\mathrm{bm}}^{\mathrm{micro}}$.

The concentrations of the signalling molecules are governed by rate equations expressing mass action kinetics of receptor–ligand binding reactions. Since time scales involved in cell differentiation and apoptosis are much longer than characteristic times of receptor–ligand binding reactions, the signalling molecule concentrations can be solved for in a quasi-steady state (adiabatic approximation) (Buenzli et al. 2012; Pivonka et al. 2012).

Explicit expressions for the signalling molecules concentrations and their modulation of the cell differentiation and apoptosis rates depending on receptor–ligand binding are presented in the sections "Differentiation rates and signalling molecules in the cell populations model" and "Recalibration of the model" of the Appendix. Below, we comment in more detail on new features of Eqs. (14)–(17) that are included to model the geometrical and biomechanical feedbacks on bone cell populations.

2.3.1 Geometrical feedback and turnover rate

The turnover rate of different bone microstructures is believed to be significantly influenced by geometric variables in particular by the availability of bone surfaces (Parfitt 1983; Martin 1972). Active osteoclasts and active osteoblasts require a surface to resorb or form bone matrix. In a fixed RVE, the more surface there is, the more cells process bone matrix, and the higher the turnover rate. A remarkable relationship between the density of bone surface $\mathrm{S_V}$ and bone volume fraction f_{bm} has been exhibited in bone tissues across wide ranges of porosities (Martin 1984; Fyhrie and Kimura 1999; Lerebours et al. 2015). This relationship $\mathrm{S_V}(f_{\mathrm{bm}})$ is particularly interesting from a computational modelling perspective as it enables to model the influence of bone surface density through an implicit dependence on bone volume fraction. Turnover rate may also be influenced by bone volume fraction in another way. Indeed, turnover rate is influenced by the biochemical microenvironment, such as the availability of precursor cells. In the femur midshaft, the availability of precursor cells depends on pore size and the radial position in the midshaft (i.e. periosteal, intracortical and endosteal), which are both well characterised by bone volume fraction. These two geometrical influences (surface density and pore size/location) can thus be represented by a single dependence of turnover rate on bone volume fraction.

In our model, different turnover rates, Eq. (13), can be achieved in microstructures of different bone volume fractions by assuming that $\mathrm{OB_u}$ and $\mathrm{OC_u}$ are functions of f_{bm}. Indeed, the functions $\mathrm{OB_u}(f_{\mathrm{bm}})$ and $\mathrm{OC_u}(f_{\mathrm{bm}})$ introduce a dependence of the active bone cell populations $\mathrm{OC_a}$ and $\mathrm{OB_a}$ upon f_{bm} via Eqs. (14)–(17). We emphasise that an explicit geometrical influence of microstructure is only introduced here on the population of uncommitted cells. This is consistent with the conclusions of Pivonka et al. (2013) who investigated different possibilities on how geometrical feedback can affect various stages of bone cell differentiation. This is also consistent with the interpretation that the microstructure's surface area plays an important role for the initiation of new BMUs (basic multicellular units), occurring through $\mathrm{OB_u}$ and $\mathrm{OC_u}$ differentiation, rather than for the activation of osteoclasts and osteoblasts. The activation of osteoclasts and osteoblasts depends instead on temporary BMU cavity internal surfaces that only comprise a small fraction of the microstructure's bone surface.

To determine functions $\mathrm{OB_u}(f_{\mathrm{bm}})$ and $\mathrm{OC_u}(f_{\mathrm{bm}})$ that lead to physiological turnover rates at different bone volume fractions, we assume that in a 'normal healthy state', a phenomenological relationship $\overline{\chi_{\mathrm{BV}}}(f_{\mathrm{bm}})$ can be defined between turnover rate and bone volume fraction, such that $\chi_{\mathrm{BV}}(\boldsymbol{r}, t) = \overline{\chi_{\mathrm{BV}}}\big(f_{\mathrm{bm}}(\boldsymbol{r}, t)\big)$. A normal healthy state is

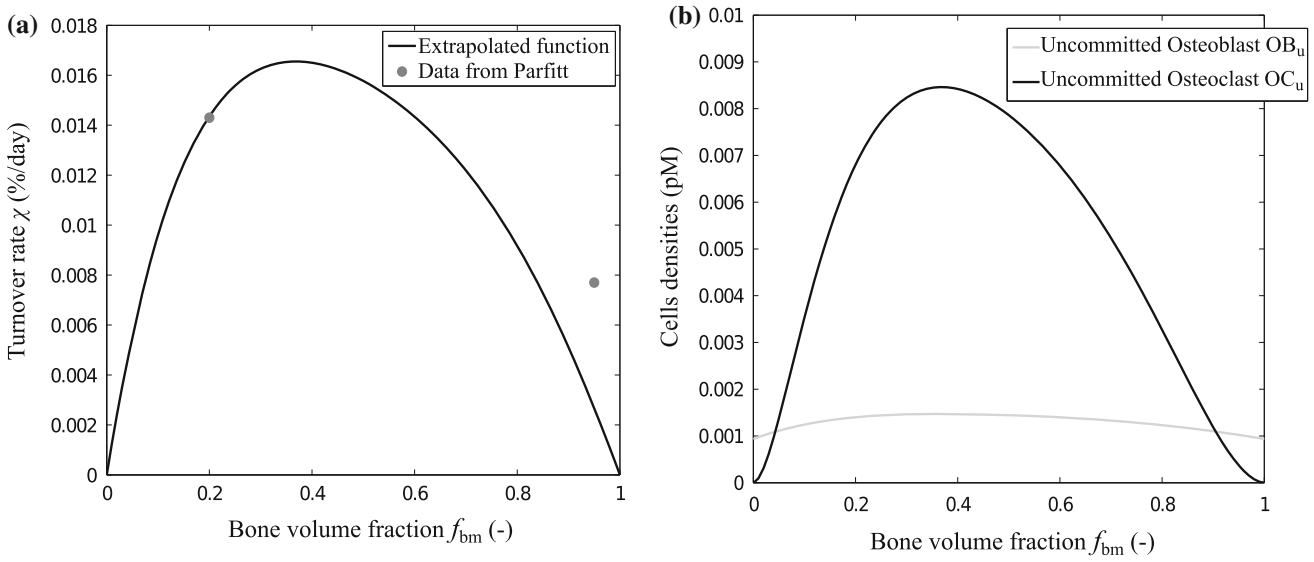

Fig. 5 **a** Plot of the phenomenological relationship $\overline{\chi_{BV}}(f_{bm})$ between turnover rate and bone volume fraction assumed in the model, the grey data points are the ones given by Parfitt (1983). **b** Dependence of OC_u and OB_u upon f_{bm} based on the prescribed bone turnover function. $OB_u(f_{bm})$ and $OC_u(f_{bm})$ serve as input values in the bone cell population model

defined as a steady state in which resorption and formation are balanced in an individual with normal physical activity and normal hormonal levels. Taking as input such a phenomenological relationship $\overline{\chi_{BV}}(f_{bm})$, one can determine for each f_{bm} the values $OC_u(f_{bm})$ and $OB_u(f_{bm})$ that lead to (i) balanced remodelling and (ii) an actual steady-state turnover rate χ_{BV} such that $\chi_{BV} = \overline{\chi_{BV}}(f_{bm})$. From Eqs. (12) and (13), this imposes the following two constraints to be solved for $OC_u(f_{bm})$ and $OB_u(f_{bm})$:

$$\overline{\chi_{BV}}(f_{bm}) = k_{form}\overline{OB_a}\big(OC_u(f_{bm}), OB_u(f_{bm})\big) \quad (18)$$

$$= k_{res}\overline{OC_a}\big(OC_u(f_{bm}), OB_u(f_{bm})\big), \quad (19)$$

where the bars on the right-hand side indicate steady-state values of the cell density variables.

By analogy with the relationship $S_V(f_{bm})$, we assume in this paper that the phenomenological relationship $\overline{\chi_{BV}}(f_{bm})$ is a dome-shaped function whose height is adjusted to Parfitt's reported measurements of turnover rate in cortical and trabecular bone (Parfitt 1983, Table 1 and Table 7),[2] see Fig. 5a. The relationship satisfies $\overline{\chi_{BV}}(0) = \overline{\chi_{BV}}(1) = 0$ since there is no turnover possible without the presence of bone surfaces. The maximum of bone turnover is assumed to occur at $f_{bm} = 0.35$, corresponding to typical trabecular or trabecularised bone microstructures in the midshaft femur. With this assumed relationship $\overline{\chi_{BV}}(f_{bm})$, the constraints (18)–(19) were solved numerically for $OB_u(f_{bm})$ and $OC_u(f_{bm})$ at each value of $f_{bm} \in [0, 1]$ by using a trust-region dogleg method. The functions $OC_u(f_{bm})$ and $OB_u(f_{bm})$ obtained by this procedure are shown in Fig. 5b. These functions are used as input in Eqs. (14)–(17) in all our simulations. This ensures that in the normal healthy state, each RVE of the midshaft cross section located at $\boldsymbol{r}$ remodels at rate $\overline{\chi_{BV}}(f_{bm}(\boldsymbol{r}))$ without changing bone volume fraction. The functions $OC_u(f_{bm})$ and $OB_u(f_{bm})$ are assumed to hold unaffected in the various deregulating circumstances considered later on (i.e. osteoporosis and altered mechanical loading). During these deregulating circumstances, the value of the actual turnover rate, Eq. (13), differs from the value of $\overline{\chi_{BV}}$ and depends implicitly on the hormonal and mechanical states that influence the active cell populations OB_a and OC_a.

The explicit calibration of the cell population model, Eqs. (14)–(17), to site-specific tissue remodelling rates is a significant novelty compared to our previous temporal model (Pivonka et al. 2013; Scheiner et al. 2013). This modification was made necessary to consistently describe the site-specific evolution of bone in the spatio-temporal framework of Buenzli et al. (2013) while retaining a cell population model that includes biochemical regulations.

2.3.2 *Mechanical feedback and initial bone microstructure stability*

A mechanical feedback is included in the cell population model such that underloaded regions of bone promote osteoclastogenesis and overloaded regions of bone promote osteoblastogenesis (Frost 1987, 2003). These responses are viewed as consequences of biochemical signals transduced

[2] Parfitt reports that cortical bone of average bone volume fraction 0.95 has a turnover rate of $0.115\,cm^3/day$, corresponding to $\overline{\chi_{BV}}(0.95) \approx 0.77 \times 10^{-4}/day$ with $TV^{cort} = 1.5 \times 10^6\,mm^3$. He also reports that trabecular bone of average bone volume fraction 0.20 has a turnover rate of $0.25\,cm^3/day$, corresponding to $\overline{\chi_{BV}}(0.20) \approx 1.43 \times 10^{-4}/day$ with $TV^{trab} = 1.75 \times 10^6\,mm^3$.

from a mechanical stimulus sensed by osteocytes (Bonewald 2011). Osteocytes are known to express RANKL, which regulates osteoclast generation, and sclerostin, which regulates osteoblast generation via Wnt signalling (Bonewald and Johnson 2008). Following Scheiner et al. (2013), the resorptive response of the mechanical feedback is assumed to act by an increase in the microenvironmental concentration of RANKL, whereas its formative response is assumed to act by an increase in the proliferation rate of osteoblast precursors.

The exact nature of the mechanical stimulus sensed by osteocytes is still a matter of debate. It may include lacunocanalicular extracellular fluid shear stress on the osteocyte cell membrane, extracellular fluid pressure, streaming potentials and direct deformations of the osteocyte body induced by bone matrix strains (Knothe Tate 2003; Bonewald and Johnson 2008; Bonewald 2011). Due to the extensive network of osteocyte connections in bone (Buenzli and Sims 2015), average bone matrix strains at a higher scale may also be sensed by the osteocyte network. Below, we assume that the mechanical stimulus to the bone cell population model is described by a local strain energy density, $\Psi(\boldsymbol{r}, t)$. This strain energy density will be taken to be either the microscopic, cellular-scale strain energy density of bone matrix, $\Psi_{\mathrm{bm}}^{\mathrm{micro}}(\boldsymbol{r}, t)$, or the average tissue-scale strain energy density, $\Psi^{\mathrm{tissue}}(\boldsymbol{r}, t)$, defined, respectively, in Eqs. (11) and (10).

To predict with our model the evolution of a real scan of midshaft femur under various deregulating circumstances, it is important to assume that the bone scan represents a stable state initially in the absence of any deregulation. In particular, this initial bone state is assumed mechanically optimal. This can be ensured by choosing the local mechanical stimulus acting onto the bone cells, $\mu(\boldsymbol{r}, t)$, as a normalised difference between the current SED and the SED of the initial bone microstructure $\Psi(\boldsymbol{r}, 0)$:

$$\mu(\boldsymbol{r}, t) = \frac{\Psi(\boldsymbol{r}, t) - \Psi(\boldsymbol{r}, 0)}{\Psi(\boldsymbol{r}, 0) + K} \tag{20}$$

The normalisation by $\Psi(\boldsymbol{r}, 0)$ in the denominator in Eq. (20) ensures that the mechanical stimulus is not over-emphasised away from the neutral axis where SED takes high values. The small positive constant $K = 1 \cdot 10^{-6}$ GPa is added to keep mechanical stimulus well defined near the neutral axis where $\Psi(\boldsymbol{r}, 0) \approx 0$ (see also Discussion Sect. 4.3).

When negative, $\mu(\boldsymbol{r}, t)$ in Eq. (20) is assumed to promote $\beta_{\mathrm{RANKL}}^{\mathrm{mech}}$, the production rate of RANKL (Fan et al. 2004; Wang et al. 2004):

$$\beta_{\mathrm{RANKL}}^{\mathrm{mech}}(\Psi) = \begin{cases} -\kappa \cdot \mu(\boldsymbol{r}, t), & \text{if } \mu(\boldsymbol{r}, t) \le 0 \\ 0, & \text{if } \mu(\boldsymbol{r}, t) > 0 \end{cases} \tag{21}$$

where κ is a parameter describing the strength of the biomechanical transduction (see Sect. 2.6). This results in increased RANKL signalling in underloaded conditions (see Eq. (28) in Appendix), and so in increased osteoclast generation in Eqs. (14)–(15).

When positive, $\mu(\boldsymbol{r}, t)$ in Eq. (20) is assumed to promote $\mathcal{P}_{\mathrm{OB_p}}$, the proliferation rate of pre-osteoblasts in Eq. (16) (Kaspar et al. 2002; Weyts et al. 2003; Robling et al. 2006):

$$\mathcal{P}_{\mathrm{OB_p}}(\Psi) = P_{\mathrm{OB_p}} + \begin{cases} 0, & \text{if } \mu(\boldsymbol{r}, t) \le 0 \\ P_{\mathrm{OB_p}} \cdot \lambda \cdot \mu(\boldsymbol{r}, t), & \text{if } 0 < \mu(\boldsymbol{r}, t) < \frac{1}{\lambda} \\ P_{\mathrm{OB_p}}, & \text{if } \mu(\boldsymbol{r}, t) \ge \frac{1}{\lambda} \end{cases} \tag{22}$$

where λ is a parameter describing the strength of the biomechanical transduction. The first term in (22) accounts for a transit-amplifying stage of osteoblast differentiation occurring in the absence of mechanical stimulation (Buenzli et al. 2012). The proliferation rate is assumed to saturate to the value $\mathcal{P}_{\mathrm{OB_p}} = 2P_{\mathrm{OB_p}}$ in highly overloaded situations to ensure the stability of the population of $\mathrm{OB_p}$s (Buenzli et al. 2012; Scheiner et al. 2013).

A similar type of mechanical feedback was implemented in purely temporal settings in Scheiner et al. (2013). The initial SED distribution, $\Psi(\boldsymbol{r}, 0)$, is calculated from Eqs. (10)–(11) and from the initial bone volume fraction distribution, $f_{\mathrm{bm}}(\boldsymbol{r}, 0)$, determined on the bone scan (described in the next section).

2.4 Initial distribution of bone volume fraction from microradiographs

The initial microstructural state of the midshaft bone cross section can be derived from high-resolution bone scans such as microcomputed tomography (micro-CT) scans or microradiographs. Since Haversian canals have an average diameter of about 40 µm, at least 10-µm resolution is required to evaluate intracortical bone volume fractions with sufficient accuracy.

In the simulations presented in Sect. 3, we used the microradiograph represented in Fig. 6a where the pixel size is 7 µm. The femur sample was collected from a 21-year-old subject. The microradiograph was digitised and binarised by a thresholding operation based on pixel grey level. Bone matrix is assigned the value 1 irrespective of the degree of mineralisation, and intracortical pores are assigned the value 0. The distribution of the bone volume fraction, $f_{\mathrm{bm}}(\boldsymbol{r}, 0)$, across the midshaft was determined by calculating the volume of bone matrix in a disc of 2 mm diameter, centred at each pixel of the binarised image and divided by the disc's area. For the points near the periosteal surface, only the portion of the disc contained into the subperiosteal area was used for this calculation (see Fig. 6b). The discrete values of f_{bm} defined at each pixel contained in the subperiosteal region were then interpolated

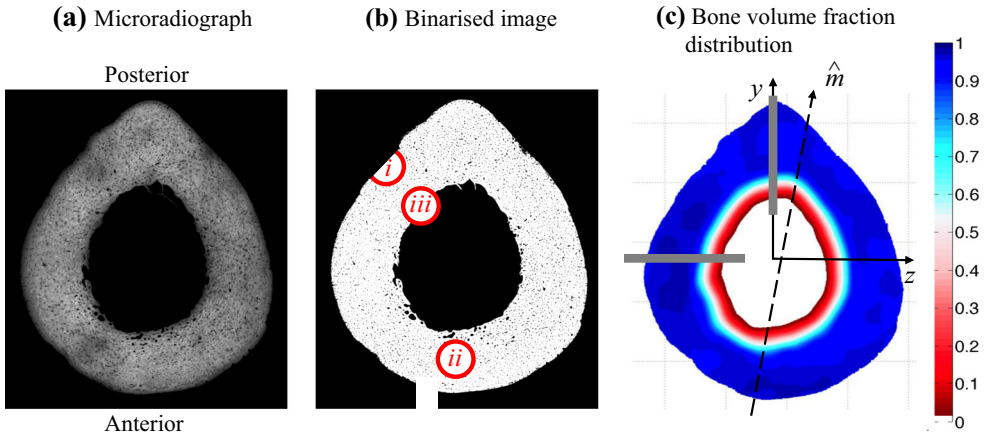

Fig. 6 **a** Microradiograph of a midshaft femur cross section (courtesy of C. David L. Thomas and John G. Clement, Melbourne Femur Collection). **b** Binarisation of the microradiograph and determination of the local f_{bm} values: (i) at the periosteal region; (ii) in the intracortical region; and (iii) at the endosteal region; **c** Bone volume fraction distribution extracted from the radiograph and interpolated. The dashed line represents the location of the neutral axis. The origin of the coordinate system (y, z) is taken at the normal force centre, NC. The grey lines are the 10 mm along which we are studying the evolution of the model in the Results Section

into a continuous function, $f_{\mathrm{bm}}(\boldsymbol{r}, 0)$, using MATLAB's 2D cubic interpolation procedure. The result is shown in Fig. 6c. A similar exclusion was not performed at the endosteal surface since this surface is less well defined, in opposition to the periosteal surface, due to the presence of trabecular-like structures. Bone matrix volume fractions near the endosteal surface are averages of intracortical bone regions and regions in the bone marrow cavity.

2.5 Numerical simulations

The multiscale mechanobiological model of bone remodelling presented in this paper is governed by a coupled system of (i) distributed ODEs describing the evolution of bone cell populations at each location $\boldsymbol{r}$ in the midshaft femur (Eqs. (14)–(17)) and (ii) non-local and tensorial algebraic equations determining the mechanical state of the tissue RVE at $\boldsymbol{r}$, both at the tissue scale and at the microscopic scale (Eqs. (2)–(11)). The model is initialised with a bone volume fraction distribution across the midshaft femur deduced from high-resolution bone scans (Fig. 6a) and with steady-state populations of cells fulfilling the site-specific turnover rate conditions Eqs. (18)–(19). This initial state is thereby constructed to be a steady state of the model, in which the biochemical, geometrical and mechanobiological regulations of resorption and formation are balanced.

To solve this non-local spatio-temporal problem numerically, we use a staggered iteration scheme in which we first solve the mechanical problem (i.e. tissue-scale SED and microscopic SED), assuming constant material properties, and then solve the bone cell population model and evolve the bone volume fraction at each location $\boldsymbol{r}$ of the femur midshaft assuming constant mechanical feedback for a duration Δt. After Δt, the mechanical problem is recalculated based on the updated bone volume fraction distribution, $f_{\mathrm{bm}}(\boldsymbol{r}, \mathrm{t}+\Delta\mathrm{t})$, and this procedure is iterated. The ODEs are solved using a standard stiff ODE solver (MATLAB, ode15s). The spatial discretisation is a regular grid with steps $\Delta y = \Delta z = 0.8$ mm. Due to the separation of time scales between changes in the local mechanical environment (years) and changes in bone cell populations (days), the mechanical stimulus requires updating after durations Δt = 2 years. The accuracy of the numerical results depending on Δt is studied in the section "Update frequency of mechanical state in the numerical algorithm" of the Appendix.

2.6 Model calibration

The model presented in this paper contains: (i) biomechanical parameters associated with the estimation of $\Psi(\boldsymbol{r}, t)$, and (ii) parameters associated with the bone cell population model. Biomechanical parameters as well as biochemical parameters were determined and validated in other studies (Scheiner et al. 2013; Pivonka et al. 2013, 2008; Buenzli et al. 2012) (Table 1). The origin and robustness of parameter estimates are discussed in the section "Model parameter values" of the Appendix. Here we calibrate the newly introduced parameters: (a) mechanical coupling parameters λ and κ (Eqs. (21) and (22)), and (b) biochemical parameters related to the simulation of osteoporosis.

2.6.1 *Calibration of the hormonal deregulation for osteoporosis simulation*

In our previous temporal model (Scheiner et al. 2013), osteoporosis was modelled by an increase in systemic PTH together

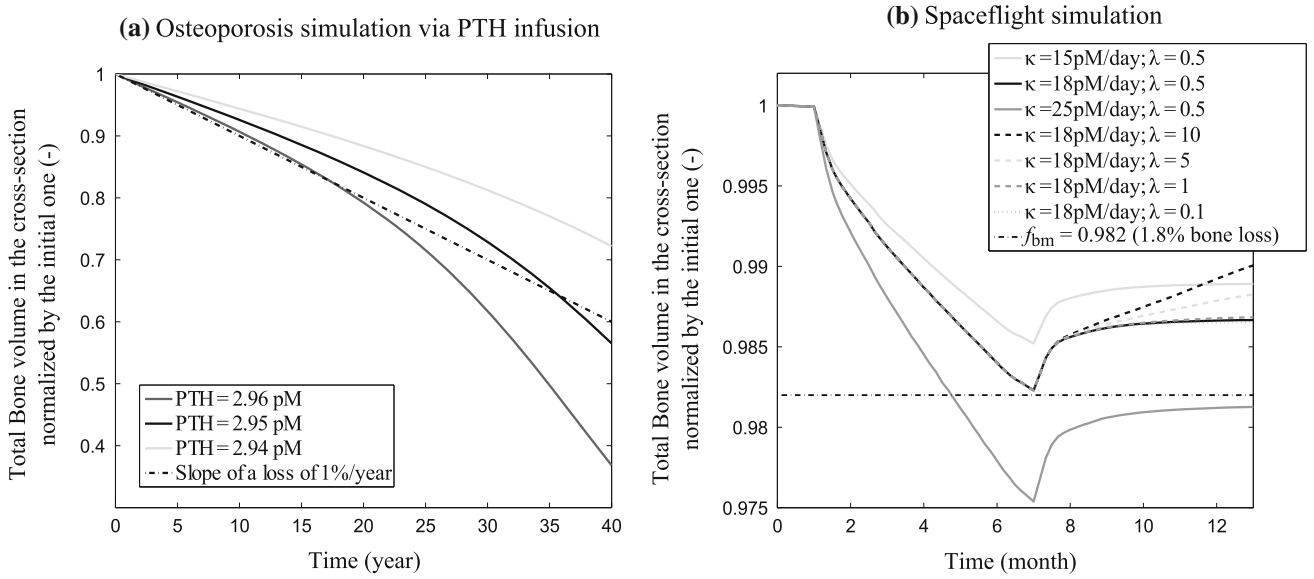

Fig. 7 **a** Evolution of the total bone mass in the cross section with time while simulating osteoporosis: calibration of the PTH infusion. Osteoporosis is characterised by a bone loss of 1 %/year (Parfitt and Chir 1987; Nordin et al. 1988; Szulc et al. 2006). **b** Evolution of the total bone mass in the cross section with time while simulating a spaceflight mission: calibration of the mechanical parameters, λ and κ

with a reduction in the biomechanical transduction parameters: λ and κ. In this paper, we simulate age-related bone loss using a single parameter perturbation, i.e. an increase in systemic PTH concentration. This increase is calibrated so as to obtain a loss of total bone cross-sectional area in the femur midshaft of 1 % per year [3] (Parfitt and Chir 1987; Nordin et al. 1988; Szulc et al. 2006). The total bone cross-sectional area is defined by the integral of $f_{\text{bm}}(\boldsymbol{r}, t)$ over the midshaft cross section. In the model, a rate of bone loss of 1 %/year was obtained by an increase in systemic concentration of PTH from 2.907 to 2.954 pM (1.62 % increase) (see Fig. 7a).

2.6.2 *Calibration of mechanobiological feedback*

The rate of change in bone mass due to mechanical feedback is determined in the model by the biomechanical transduction parameters λ (in Eq. (22)) and κ (in Eq. (21)). To calibrate these parameters, we used data gathered from mechanical disuse and re-use experiments. It has been shown that cosmonauts undertaking long mission space flights lose bone mass at a rate of approximately 0.3 % per month (Vico et al. 2000). This microgravity-induced bone loss is only slowly recovered after return to Earth. No significant bone gain is observed after 6-month exposure to normal gravity on Earth (Vico et al. 2000; Collet et al. 1997).

In our multiscale model, microgravity is simulated as a 80 % reduction in the normal mechanical loads experienced by the femur, i.e. $\boldsymbol{N}_{\text{microgravity}} = 0.2\boldsymbol{N}$ and $\boldsymbol{M}_{\text{microgravity}} = 0.2\boldsymbol{M}$. Based on these reduced loads, the parameter κ has been calibrated such that 1.8 % of total bone cross-sectional area is lost after 6 months. We found such rate of loss with $\kappa = 18$ pM/day when the mechanical stimulus is based on the microscopic SED, $\Psi_{\text{bm}}^{\text{micro}}(\boldsymbol{r}, t)$ (see Fig. 7b), and $\kappa = 19$ pM/day when the mechanical stimulus is based on the tissue-scale SED, $\Psi^{\text{tissue}}(\boldsymbol{r}, t)$. After return to Earth, rates of bone recovery are too low to be detected after 6 months (Collet et al. 1997). We performed a parametric study investigating various strengths of λ. Using parameter values of $\lambda > 1$ in our model results in significant bone gain after 6 months, while $\lambda \leq 1$ results in small bone gain. Based on these results, we use $\lambda = 0.5$ for both the microscopic and tissue-scale mechanical stimuli.

3 Results

In this section, we present numerical simulations of the evolution of the midshaft femur cross section subjected to either (i) changes in mechanical environment (Sect. 3.1) or (ii) hormonal deregulation simulating osteoporosis (Sect. 3.2). We also investigate how site-specific bone loss may depend on whether mechanical stimulus is sensed at the microscopic, cellular scale or at the tissue scale.

3.1 Bone loss due to mechanical disuse

Figure 8a represents site-specific changes of the femur midshaft cross section simulated by the model assuming a 80 %

[3] The calibration is performed without mechanical adaptation (i.e. setting $\lambda = 0$ and $\kappa = 0$ in Eqs. (21) and (22)) in order to compare both mechanical feedbacks in a more consistent way.

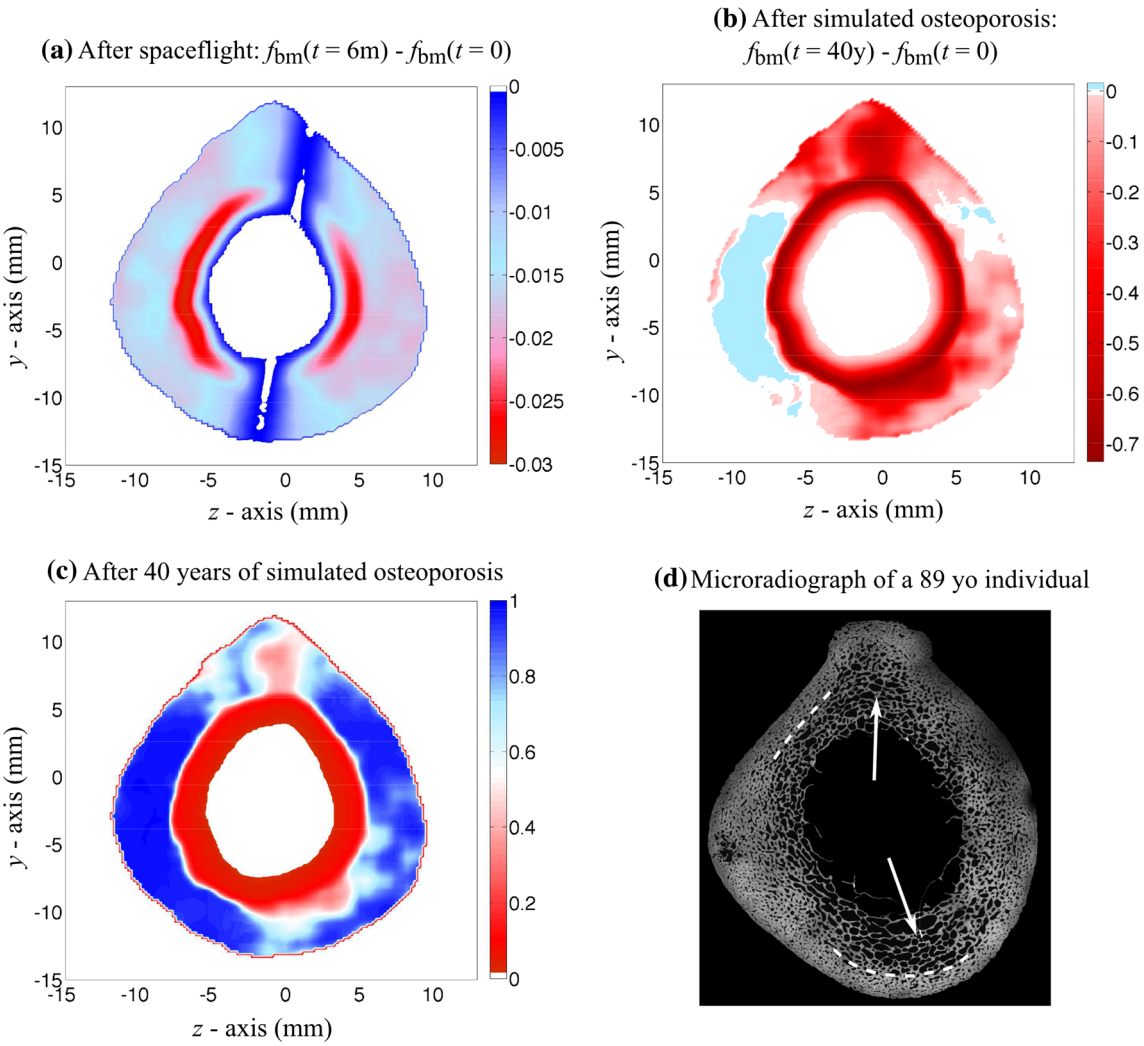

Fig. 8 **a** Difference between the bone volume fraction distribution in the cross section after a 6-month spaceflight mission with the initial distribution. **b** Difference between the bone volume fraction distribution in the cross section after a 40 years of simulated osteoporosis with the initial distribution. **c** Bone volume fraction distribution in the cross section after 40 years of simulated osteoporosis. **d** Microradiograph of a human femur cross section from an 89-year-old individual. The *dashed lines* highlight regions with sharp transition between porous and compact tissue. The *arrows* point out regions with high porosity along the antero-posterior axis

reduction in the normal mechanical loading. This reduction in mechanical loading may represent microgravity in long spaceflight missions (see Sect. 2.6) or prolonged bed rest. The Figure depicts the difference between the bone volume fraction distribution after 6 months of mechanical disuse and the initial bone volume fraction. It can be seen that bone loss is site-specific with more bone loss occurring near the endosteal surface. Close to the neutral axis, only limited loss of bone is observed.

3.2 Simulation of osteoporosis due to hormonal deregulation

Figure 8b and c represents the site-specific changes of the midshaft cross section that occur after 40 years of simulated osteoporosis when the mechanical feedback acting onto the bone cell population model is based on the microscopic SED. Figure 8b depicts the difference between the f_{bm} distribution at the end of the simulation and the initial distribution. Figure 8c depicts the f_{bm} distribution at the end of the simulation. Bone loss occurs everywhere in the cross section except at the medial and lateral sides. The loss is site specific with higher rates of loss in the endocortical region and around the neutral axis, close to the antero-posterior axis. This pattern of bone loss is consistent with the high porosity commonly observed in these regions in osteoporotic subjects (Fig. 8d, arrows). The simulation exhibits a sharp transition between a very porous endocortical region and a dense intracortical region towards the periosteum. Although perhaps less pronounced, such a transition is also observed in the microradiograph of Fig. 8d (dashed lines). In contrast to the osteoporosis simulation, the simulation of mechanical disuse (Fig. 8a) shows

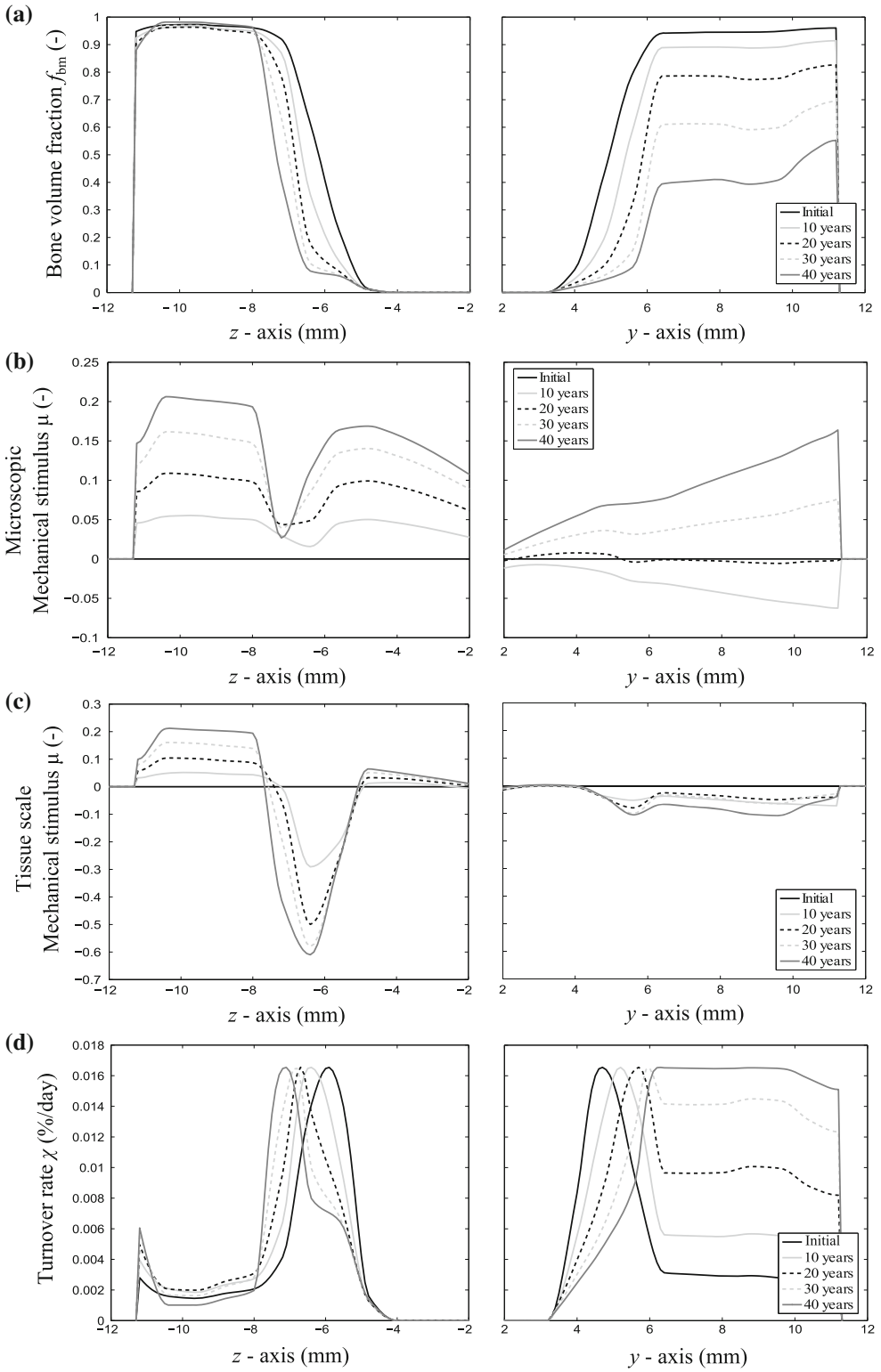

Fig. 9 Evolution of **a** bone volume fraction; **b** mechanical stimulus, $\mu(\boldsymbol{r}, t)$, at the microscopic scale; **c** mechanical stimulus, $\mu(\boldsymbol{r}, t)$, at the tissue scale; and **d** turnover rate along the y and z-axis during the simulation of osteoporosis

that bone was lost all over the cross section, with little change around the neutral axis. In both simulations, bone was lost predominantly in the endocortical region.

In Fig. 9, we show how the distributions of the following quantities evolved along the y- and the z-axes during the simulation of osteoporosis: (a) the bone volume frac-

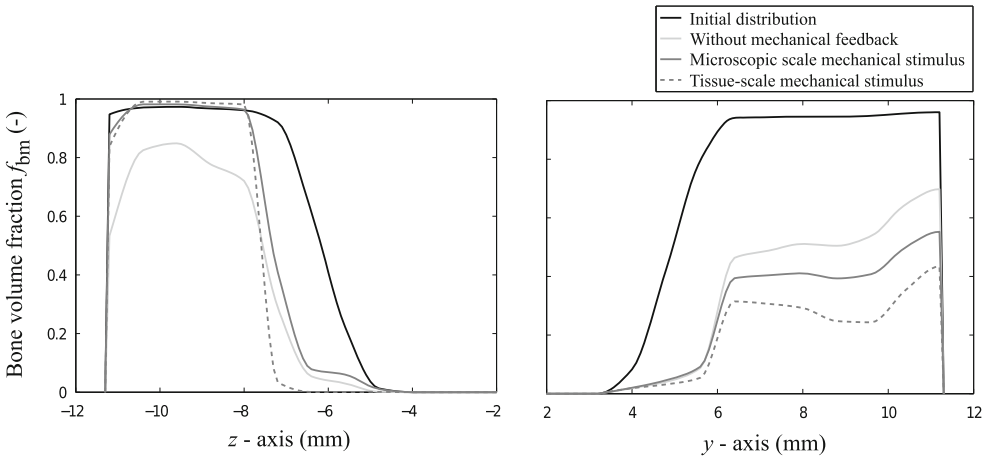

Fig. 10 Bone volume fraction along the y- and z-axes, the initial distribution and the distributions after 40 years of simulated osteoporosis, without mechanical regulation, with mechanical regulation based on microscopic SED and with mechanical regulation based on tissue-scale SED

tion, (b) the microscopic mechanical stimulus, $\mu_{\mathrm{bm}}^{\mathrm{micro}}$, used as mechanical stimulus in this simulation, (c) the tissue-scale mechanical stimulus, μ^{tissue}, not used as mechanical stimulus in this simulation and (d) the turnover rate. Along both axes, the regions in which bone volume fraction transitions from low to high ($3 < y < 6\,\mathrm{mm}$ and $-7 < z < -5\,\mathrm{mm}$) are resorbed at higher rate, due to the higher values of χ_{BV} in these regions (Fig. 9d). As time progresses, bone volume fraction is strongly reduced in the endocortical region, leading to an expansion of the marrow space and a reduction in cortical wall width. This is accompanied by a shift of the maximum of χ_{BV} towards the periosteum. Along the y-axis (near the neutral axis), bone is lost at a high rate not only in the endocortical region but also near the periosteum, as can be seen by the gradual increase in turnover rate in the whole cortical width (Fig. 9d). In contrast, along the z-axis, bone is lost at a high rate only at the endosteum where turnover rate maintains a well-defined peak. The intracortical region ($z < -7\,\mathrm{mm}$) is preserved even after 40 years of simulated osteoporosis.

3.2.1 Microscopic vs tissue-scale mechanical stimulus

Comparing Fig. 9b and c, we can observe that the values of the mechanical adaptation stimuli are strongly dependent on the length scale at which they are calculated, i.e. tissue scale or microscopic scale. Along the z-axis, $\mu_{\mathrm{bm}}^{\mathrm{micro}}$ is always positive (Fig. 9b), whereas, μ^{tissue} takes negative values in the endocortical region (Fig. 9c). Regions with high values of $\mu_{\mathrm{bm}}^{\mathrm{micro}}$ and positive values of μ^{tissue} correlate with regions where the bone matrix is preserved. Regions with low values of $\mu_{\mathrm{bm}}^{\mathrm{micro}}$ and negative values of μ^{tissue} correlate with regions where the bone matrix is resorbed. The Figures also show a qualitative and quantitative difference in mechanical stimuli $\mu_{\mathrm{bm}}^{\mathrm{micro}}$ and μ^{tissue} between the y- and z-axes. The mechanical stimulus is asymmetric between the antero-posterior axis and lateral–medial axis due to the assumed bending loading state. Along the y-axis, no important variation can be observed between endocortical and periosteal regions. Along the z-axis, both stimuli exhibit much lower values in the endocortical region than at the periosteum or in the marrow cavity. We note that the mechanical stimuli are not zero in the marrow even when $f_{\mathrm{bm}} = 0$ due to the assumed vascular stiffness.

Figure 10 compares the evolution of bone volume fraction during simulated osteoporosis when the mechanical stimulus acting onto the bone cells is either (i) absent, (ii) based on the microscopic mechanical stimulus, $\mu_{\mathrm{bm}}^{\mathrm{micro}}$, or (iii) based on the tissue-scale mechanical stimulus, μ^{tissue}.[4] All cases exhibit strong endocortical bone loss with little difference in the expansion rate of the medullary cavity. A slightly steeper endosteal wall is created along the z-axis during the simulation using tissue-scale mechanical stimulus, and a region with very low bone volume fraction ($f_{\mathrm{bm}} \simeq 0.1$) is preserved in the medullary cavity during the simulation with microscopic mechanical stimulus. Intracortical bone towards the periosteum is preserved along the z-axis by both mechanical stimuli, but it is resorbed more strongly along the y-axis in the simulation with tissue-scale mechanical stimulus.

4 Discussion

4.1 Endocortical bone loss

The loss of endocortical bone, with its associated expansion of the marrow cavity and cortical wall thinning, is a

[4] For the simulation in case (iii), the mechanical transduction strength parameters are: $\kappa = 19$ pM/day and $\lambda = 0.5$, calibrated with the tissue-scale mechanical stimulus while simulating spaceflight.

trait common to several bone disorders and deregulations of remodelling. It is observed in biochemical disorders, such as in osteoporosis, vitamin D deficiency and hyperparathyroidism (Feik et al. 1997; Parfitt 1998; Bousson et al. 2001; Thomas et al. 2005; Szulc et al. 2006; Zebaze et al. 2010; Busse et al. 2013; Hirano et al. 2000; Burr et al. 2001; Turner et al. 2002). It is also observed during disruptions of normal mechanical loading, such as in prolonged bed rest, long-term space missions and trauma-induced paralysis such as spinal cord injury (Leblanc et al. 2007; Rittweger et al. 2009; Vico et al. 2000; Lang et al. 2004; Kiratli et al. 2000; Eser et al. 2004), and in animal experiments involving muscle paralysis or hindlimb disuse induced by tail suspension (Warner et al. 2006; Ausk et al. 2012, 2013; Bloomfield et al. 2002; Judex et al. 2004).

Our numerical simulations of osteoporosis and mechanical disuse are consistent with these experimental findings. All Figs. 8, 9 and 10 highlight the strong site-specificity of bone loss under deregulations of bone remodelling. The endocortical region systematically undergoes the most significant loss. This similarity arises despite the fact that in the simulation of mechanical disuse, the deregulation is non-uniform in the cross section (due to the uneven distribution of mechanical loads), whereas in the simulation of osteoporosis, the hormonal deregulation is uniform in the cross section.

The precise mechanisms that underlie the predominant loss of bone in the endocortical region are still poorly understood (Raisz and Seeman 2001; Thomas et al. 2005; Squire et al. 2008; Ausk et al. 2012). Mechanical adaptation has been suggested as a potential mechanism (Frost 1997; Burr 1997; Thomas et al. 2005; Jepsen and Andarawis-Puri 2012). Bone loss induced by mechanical disuse redistributes mechanical loads towards the periosteum, where bone volume fraction is higher. This could unload endocortical regions and thereby accelerate their resorption. Reduced physical activity and muscle strength in ageing subjects support this hypothesis (Frost 1997). However, the ubiquity of endocortical bone loss in situations in which mechanical loading is not significantly modified suggests that other mechanisms are at play. The morphological influence of the tissue microstructure on the rate of bone loss has been suggested to be another important factor (Martin 1972; Squire et al. 2008; Zebaze et al. 2010; Buenzli et al. 2013). Cortical bone has little bone surface available to bone cells, but this surface expands during bone loss, which could increase the activation frequency of remodelling events. If remodelling is imbalanced, this may lead to an acceleration of bone loss and to an increase of the available surface until the tissue microstructure becomes so porous that its surface area reduces with further loss (Martin 1972; Raisz and Seeman 2001).

We have shown previously the possibility of this morphological mechanism to explain cortical bone trabecularisation in both temporal (Pivonka et al. 2013) and spatio-temporal settings (Buenzli et al. 2013). The spatio-temporal model proposed in the present work incorporates both mechanical adaptation and a morphological feedback of the microstructure on turnover rate. In Fig. 10, our simulations of osteoporosis conducted with and without mechanical feedback suggest that the rate at which the medullary cavity expands and the cortical wall thins is only marginally dependent on mechanical adaptation. This rate is primarily due to the high turnover rates present in the endocortical region (Fig. 9d), i.e. due to the morphological influence of microstructure on the rate of loss. This proposed mechanism is consistent with the observation that distinct conditions exhibit endocortical bone loss, whether mechanical loading is disrupted or not.

4.2 Model formulation of morphological feedback

In the cell population model of Pivonka et al. (2013), the morphological influence of the tissue microstructure was included through the specific surface of the tissue (Martin 1984; Lerebours et al. 2015) normalised by its initial value. This normalisation allowed to maintain the same cell behaviour in both cortical and trabecular bones. However, it leads to a turnover rate that is initially independent of bone volume fraction, and so the same in cortical and trabecular bone. The morphological feedback proposed in the present model differs by (i) avoiding a dependence on an initial reference state (i.e. absence of normalisation to allow microstructure-dependent turnover rates) and (ii) by referring to turnover rate (a dynamic biological quantity) instead of specific surface (a morphological characterisation of the microstructure).

While specific surface can be estimated directly from high-resolution scans of bone tissues (Chappard et al. 2005; Squire et al. 2008; Lerebours et al. 2015), quantitative links between S_V and cell numbers remain unclear (Martin 1972; Parfitt 1983; Pivonka et al. 2013). The direct reference to turnover rate, in the present model, makes the model more accurate, due to the straightforward link between turnover rate and cell populations (see Eq. (13)). Unfortunately, turnover rate is rarely measured experimentally by cell counts or volumes of bone resorbed and re-formed. It is most commonly characterised by measurements of serum concentrations of bone resorption and/or formation markers (Szulc et al. 2006; Burghardt et al. 2010; Malluche et al. 2012), which are difficult to relate quantitatively to cell numbers or bone volume at a particular bone site. While the phenomenological relationship $\overline{\chi_{BV}}(f_{bm})$ that we assumed between turnover rate and microstructure remains to be studied quantitatively, such a relationship has been suggested in several studies (Felsenberg and Boonen 2005; Burghardt et al. 2010; Malluche et al. 2012).

4.3 Nature of the mechanical stimulus

The nature of the mechanical stimulus sensed by bone cells and transduced into signals prompting resorption or formation has been a matter of discussion for many years. A number of computational studies simulating mechanical adaptation of bone microstructure suggested that the strain energy density could be a good candidate. Ruimerman et al. (2005) tested several mechanical stimuli and concluded the SED gave best results when comparing simulations outcomes with biological parameters such as porosity, trabecular number or adaptability to external loading. However, Levenston and Carter (1998) argued that the drawback of using the SED is that it does not lead to a different response when bone is stimulated in tension or in compression. In the literature, most computational models use the SED because it is a scalar representing both microstructure and mechanical loading (Fyhrie and Carter 1986; Mullender et al. 1994; Van Rietbergen et al. 1999; Van Oers et al. 2008; Scheiner et al. 2013). Quantitative criteria based on experimental observations are still lacking, especially ones testing the tensorial aspects of mechanical loading conditions. For our purpose of studying tissue-scale average changes in bone volume fraction, these tensorial aspects are likely to be secondary. Hence, we have based our mechanical stimulus on the strain energy density (see below for a discussion of the scale). We note here that other mechanical quantities have also been proposed and studied for their magnitude and possible influence onto osteocytes, such as fluid shear stress and fluid pressure in the lacuno-canalicular system (Knothe Tate et al. 1998; Burger et al. 2003; Tan et al. 2007; Bonewald and Johnson 2008; Adachi et al. 2009b).

Mechanical adaptation also relies on the comparison of the current mechanical state with a reference state. The definition of this reference state remains unclear (Frost 1987; Carter and Beaupré 2001). Our choice is to take as mechanical reference state the initial distribution of the strain energy density in the midshaft femur. This choice introduces a memory of the stimulus "normally" experienced in a certain region of the tissue. This memory effect leads to a position-dependent reference state which can be interpreted as taking into account different sensitivities of the mechano-sensing cells depending on where they are located (Skerry et al. 1988; Turner et al. 2002; Robling et al. 2006).

4.4 Neutral axis and site-specific bone adaptation

A common issue in models of mechanical adaptation is the risk to resorb too much bone in regions that are naturally unloaded. Such regions may exist when bending moment is large enough with respect to compressive or tensile forces. In the human midshaft femur, a neutral axis runs approximately along the antero-posterior axis (Lanyon and Rubin 1984; Cordey and Gautier 1999; Thomas et al. 2005; Martelli et al. 2014). To prevent excessive resorption in such regions, some models have considered torsional loads (Van der Meulen et al. 1993; Carpenter and Carter 2008), average values of periodic dynamic loads under which the neutral axis moves (Van der Meulen et al. 1993; Carter and Beaupré 2001), or a residual background of mechanical stimulus modelling muscle twitching and other background mechanical forces (Mittlmeier et al. 1994; Carpenter and Carter 2008).

Such additional features were not introduced explicitly in our model. The strength of the mechanical stimulus around the neutral axis remained weak in our simulation of mechanical disuse (Fig. 8a). This is due to the fact that stimulus sensitivity is prescribed according to the initial state. The neutral axis did not move substantially during the simulation, and so the difference in strain energy density remained small. Resorption around the neutral axis was pronounced in our simulation of osteoporosis (Figs. 8b, c and 9) due to hormone-induced remodelling imbalance. Resorption was limited by the duration of the simulated osteoporosis (40 years) and the calibration of the overall bone loss according to experimental data.

The bending moment exerted onto the femur at the midshaft creates a strong asymmetry in the local mechanical state. Over time, this asymmetry leads to a cortical wall thickness which differs between the y-axis (antero-posterior axis) and the z-axis (lateral–medial axis), as seen in Fig. 9a. Asymmetries in cortical wall thickness and bone volume fraction, in osteoporotic patients, are commonly observed (Fig. 8d) (Feik et al. 2000; Thomas et al. 2005; Zebaze et al. 2010).

4.5 Microscopic versus tissue-scale mechanical regulation

Mechanical deformations of bone matrix can be sensed by osteocytes at the microscopic, cellular scale by deformation of the cell body, transmitted either through direct contact with the matrix or through changes in fluid flow or hydrostatic pressure (Weinbaum et al. 1994; Knothe Tate 2003; Adachi et al. 2009b, a; Bonewald 2011). However, osteocytes are highly connected to one another and to other cells in the vascular phase by an extensive network (Marotti 2000; Kerschnitzki et al. 2013; Buenzli and Sims 2015). While signal transmission mechanisms in this network remain to be determined, it is possible that the network integrates deformations of both the matrix and vascular phases before transducing them into a biochemical response, enabling a mechanical sensitivity of the network to tissue-average stresses and strains.

The uncertainty of the scale at which mechanical stimulus is sensed in bone has motivated many computational studies to estimate stress concentration effects in bone microstructures (Hipp et al. 1990; Kasiri and Taylor 2008; Gitman et al. 2010). However, few studies have explored the changes that

occur during simulated bone loss when using microscopic or tissue-scale mechanical stimulus.

Our simulations of osteoporosis show that most of the difference between the mechanical stimulus at the microscopic and tissue scales occurs near the endosteum and neutral axis (Fig. 9b, c). Changes in bone volume fraction were similar in both simulations. Stress concentration effects captured in the microscopic mechanical stimulus (but not in the tissue-scale mechanical stimulus) resulted in maintaining a region of low porosity ($f_{\mathrm{bm}} \simeq 0.1$) near the medullary cavity and in widening the transition between endocortical and intracortical bone volume fractions (Fig. 10).

Osteoporotic human femur midshafts exhibit a wide range of variability, reflecting the multiple factors influencing bone loss (Feik et al. 1997, 2000; Thomas et al. 2005; Zebaze et al. 2010). The expansion of the medullary cavity and thinning of the cortical wall are commonly reported, but other changes in midshaft tissue microstructures have been studied less systematically. Depending on the subject and their specific condition, the transition between porous endocortical bone and dense intracortical bone may be sharp or wide, and highly porous microstructures near the endosteum may be found or not (Feik et al. 1997, Figure 6).

Our model possesses several limitations which prevent at this stage to draw definite conclusions about the mechanical regulation of the tissue. The mechanical state is calculated only based on bone volume fraction. Other microstructural parameters such as the connectivity of the microstructure are not accounted for. Loss of connectivity is observed in osteoporotic trabecular bone (Parfitt et al. 1987; Mosekilde 1990; Raisz and Seeman 2001), which could lead to mechanical disuse and so increase in resorption. Periosteal apposition is often reported and believed to result from a compensation of endocortical bone loss in osteoporotic patients (Szulc et al. 2006; Russo et al. 2006; Jepsen and Andarawis-Puri 2012). Our simulations assumed the periosteal surface to be fixed, which could limit the expansion rate of the medullary cavity. Finally, our simulation of osteoporosis assumed a constant level of physical activity. A reduction in physical activity with age could further limit the preservation of bone matrix by mechanical feedback.

5 Summary and conclusions

In this paper, a novel spatio-temporal multiscale model of bone remodelling is proposed. This model bridges organ, tissue and cellular scales. It takes into account biochemical, geometrical and biomechanical feedbacks. The model is applied to simulate the evolution of a human femur midshaft scan under mechanical disuse and osteoporosis. It enables us to investigate how these scales and feedbacks interact during bone loss. Our numerical simulations revealed the following findings:

- Endocortical bone loss during both osteoporosis and mechanical disuse is driven to a large extent by site-specific turnover rates.
- Mechanical regulation does not influence significantly the expansion rate of the medullary cavity.
- Mechanical regulation helps preserve cortical bone near the periosteum. It explains site-specific differences in the bone volume fraction distribution in the midshaft cross section during osteoporosis such as increased porosity near the neutral axis, and thicker cortical wall along the medial–lateral axis of the femur midshaft, due to the anisotropy of the mechanical stimulus in the presence of bending moments.
- The inclusion of stress concentration effects in the mechanical stimulus sensed by the bone cells has a pronounced effect on porosity in the endocortical region.

Our methodology provides a framework for the future development of patient-specific models to predict loss of bone with age or deregulating circumstances.

Acknowledgments We thank C. David L. Thomas and Prof. John G. Clement for providing the microradiographs of the femur cross sections. PRB is the recipient of an Australian Research Council Discovery Early Career Research Award (DE130101191).

Compliance with ethical standards

Conflicts of interest The authors declare that they have no conflict of interest.

Appendix 1: Complements on the model description

Differentiation rates and signalling molecules in the cell populations model

In Sect. 2.3, we presented the simplified equations of the bone cells population model. Here are the developments of these equations.

$$
\begin{aligned}
&\mathcal{D}_{\mathrm{OC_u}}\big(\mathrm{MCSF},\,\mathrm{RANKL}(\Psi,\,\mathrm{PTH})\big)\\
&\quad = D_{\mathrm{OC_u}}\pi^{\mathrm{act}}\Big(\frac{\mathrm{MCSF}}{k_{\mathrm{OC_u}}^{\mathrm{MCSF}}}\Big)\pi^{\mathrm{act}}\Big(\frac{\mathrm{RANKL}}{k_{\mathrm{OC_u}}^{\mathrm{RANKL}}}\Big),\\
&\mathcal{D}_{\mathrm{OC_p}}\big(\mathrm{RANKL}(\Psi,\,\mathrm{PTH})\big) = D_{\mathrm{OC_p}}\pi^{\mathrm{act}}\Big(\frac{\mathrm{RANKL}}{k_{\mathrm{OC_p}}^{\mathrm{RANKL}}}\Big),\\
&\mathcal{A}_{\mathrm{OC_a}}(\mathrm{TGF\beta}) = A_{\mathrm{OC_a}}\pi^{\mathrm{act}}\Big(\frac{\mathrm{TGF\beta}}{k_{\mathrm{OC_a}}^{\mathrm{TGF\beta}}}\Big),\\
&\mathcal{D}_{\mathrm{OB_u}}(\mathrm{TGF\beta}) = D_{\mathrm{OB_u}}\pi^{\mathrm{act}}\Big(\frac{\mathrm{TGF\beta}}{k_{\mathrm{OB_u}}^{\mathrm{TGF\beta}}}\Big),\\
&\mathcal{D}_{\mathrm{OB_p}}(\mathrm{TGF\beta}) = D_{\mathrm{OB_p}}\pi^{\mathrm{rep}}\Big(\frac{\mathrm{TGF\beta}}{k_{\mathrm{OB_p}}^{\mathrm{TGF\beta}}}\Big).
\end{aligned}
\tag{23}
$$

In those equations, several signalling molecules play a role: TGFβ, RANK, RANKL, OPG, MCSF and PTH. The concentra-

tions of these molecules follow the principles of mass action kinetics of receptor–ligand reactions. Due to the separation of scale between the cells differentiation and apoptosis rates and the receptor–ligand binding reactions, we solve them in a quasi-steady-state hypothesis:

$$\mathrm{PTH}(\boldsymbol{r},t)=\begin{cases}\mathrm{P_{PTH}}, & \text{without deregulation}\\ \mathrm{P_{PTH}^{OP}}, & \text{with simulated OP}\end{cases}, \tag{24}$$

$$\mathrm{TGF\beta}(\boldsymbol{r},t)=\frac{P_{\mathrm{TGF\beta}}^{\mathrm{ext}}+n_{\mathrm{TGF\beta}}^{\mathrm{bone}}\,k_{\mathrm{res}}\,\mathrm{OC_a}}{D_{\mathrm{TGF\beta}}}, \tag{25}$$

$$\mathrm{RANK}(\boldsymbol{r},t)=N_{\mathrm{OC_p}}^{\mathrm{RANK}}\,\mathrm{OC_p}, \tag{26}$$

$$\mathrm{OPG}(\boldsymbol{r},t)=\frac{P_{\mathrm{OPG}}+\beta_{\mathrm{OB_a}}^{\mathrm{OPG}}\,\mathrm{OB_a}\,\pi^{\mathrm{rep}}\left(\frac{\mathrm{PTH}}{k_{\mathrm{OB}}^{\mathrm{PTH}}}\right)}{\beta_{\mathrm{OB_a}}^{\mathrm{OPG}}\,\mathrm{OB_a}\,\pi^{\mathrm{rep}}\left(\frac{\mathrm{PTH}}{k_{\mathrm{OB}}^{\mathrm{PTH}}}\right)/\mathrm{OPG_{sat}}+D_{\mathrm{OPG}}}, \tag{27}$$

$$\mathrm{RANKL}(\boldsymbol{r},t)=\frac{\beta_{\mathrm{OB_p}}^{\mathrm{RANKL}}\,\mathrm{OB_p}+\beta_{\mathrm{RANKL}}^{\mathrm{mech}}(\Psi)}{1+k_{\mathrm{RANK}}^{\mathrm{RANKL}}\,\mathrm{RANK}+k_{\mathrm{OPG}}^{\mathrm{RANKL}}\,\mathrm{OPG}}\times\left\{D_{\mathrm{RANKL}}+\frac{\beta_{\mathrm{OB_p}}^{\mathrm{RANKL}}\,\mathrm{OB_p}}{N_{\mathrm{OB_p}}^{\mathrm{RANKL}}\mathrm{OB_p}\,\pi^{\mathrm{act}}\left(\frac{\mathrm{PTH}}{k_{\mathrm{OB}}^{\mathrm{PTH}}}\right)}\right\}^{-1}. \tag{28}$$

Model parameter values

Table 1 lists all the parameters of the model.

Most model parameters were calibrated and validated in previous studies. The stiffness tensors $\mathbb{C}_{\mathrm{bm}}^{\mathrm{micro}}$ and $\mathbb{C}_{\mathrm{vas}}^{\mathrm{micro}}$ arising in the micromechanical theory were measured by mechanical experiments (Ashman et al. 1984; Murdock 1996); see also (Fritsch and Hellmich 2007). The secretory rate k_{form}(volume of bone matrix formed per osteoblast per day) was measured in animal models (Marotti and Zallone 1976; Jones 1974). The value used here is based on osteonal data from dogs, rescaled to match human osteon dimensions (Buenzli et al. 2014). The resorption rate k_{res} (volume of bone matrix resorbed per osteoclast per day) was estimated based on the progression speed of a cortical BMU in bone and the average number of $\mathrm{OC_a}$ per BMU (Buenzli et al. 2014).

The $\mathrm{OB_a}$ and $\mathrm{OC_a}$ cell densities are calibrated in our model to give rise to site-specific turnover rates in steady state in agreement with experimental measurements (see Sect. 2.3). The parameters λ and κ related to the strength of mechanical adaptation and the parameter $\mathrm{P_{PTH}^{OP}}$ related to the rate of bone loss during osteoporosis were calibrated in Sect. 2.6 based on experimental data.

The densities and dynamical behaviours of the precursor cell types ($\mathrm{OB_p}$, $\mathrm{OB_u}$, $\mathrm{OC_p}$ and $\mathrm{OC_u}$) and of the biochemical signalling molecules (TGFβ, PTH, RANK, RANKL, OPG and MCSF) depend on all the remaining parameters, which represent binding reaction rates, differentiation rates, proliferation rates and apoptosis rates (see Table 1). These parameters were validated qualitatively in previous studies (Pivonka et al. 2008; Buenzli et al. 2012; Pivonka et al. 2013), i.e. they give rise to physiologically expected qualitative behaviours of the model. A quantitative calibration of these parameters to physiological values of precursor cell densities and molecule concentrations was not done due to the lack of experimental data. However, such a quantitative calibration is not an issue since it can be done without altering the time evolution of the model so long as the densities of the active cells ($\mathrm{OC_a}$, $\mathrm{OB_a}$) remain properly calibrated in Sect. 2.3. Indeed, in our simulations, both the signalling molecules and precursor cell densities ($\mathrm{OC_u}$, $\mathrm{OC_p}$, $\mathrm{OB_u}$, $\mathrm{OB_p}$) are effectively in a quasi-steady at all times, the former by model assumption (see Sect. 6.1) and the latter due to the slow evolution of bone adaptation (years) compared to the faster bone cell dynamics (days, weeks). To increase the value of density or concentration of a component by a factor α, one may increase its production rate by the factor α or reduce its elimination rate by the factor $1/\alpha$. To maintain the system's behaviour with this new value of density or concentration, it suffices to adjust the sensitivity of interactions with this component with the relevant parameters (such as binding reaction rate parameters). For example, to double the concentration of TGFβ without affecting how it signals $\mathrm{OC_a}$, $\mathrm{OB_u}$ and $\mathrm{OB_p}$, one may double $n_{\mathrm{TGF\beta}}^{\mathrm{bone}}$ or halve $D_{\mathrm{TGF\beta}}$ (see Eq. (25)) and then double $k_{\mathrm{OC_a}}^{\mathrm{TGF\beta}}$, $k_{\mathrm{OB_u}}^{\mathrm{TGF\beta}}$ and $k_{\mathrm{OB_p}}^{\mathrm{TGF\beta}}$ so that the ratios $\mathrm{TGF\beta}/k_{\mathrm{OC_a}}^{\mathrm{TGF\beta}}$, $\mathrm{TGF\beta}/k_{\mathrm{OB_u}}^{\mathrm{TGF\beta}}$ and $\mathrm{TGF\beta}/k_{\mathrm{OB_p}}^{\mathrm{TGF\beta}}$ in Eq. (23) have the same values. A similar approach was used in Buenzli et al. (2014) to calibrate the cell populations within a single BMU. This approach is also used in Sect. 6.3 below.

Recalibration of the model

Since $\mathrm{OC_u}$ and $\mathrm{OB_u}$ vary with f_{bm} so as to retrieve experimentally valid turnover rates, some other parameters required modification compared with previous versions of the cell population model in which $\mathrm{OC_u}$ and $\mathrm{OB_u}$ were constant and uncalibrated (Buenzli et al. 2012; Pivonka et al. 2013).

By comparing the cell densities between this model and the previously published one (Buenzli et al. 2012), we can determine scaling coefficients which allows a systematic calibration of $\pi^{\mathrm{act}}\left(\frac{\mathrm{TGF\beta}}{k_{\mathrm{OC_a}}^{\mathrm{TGF\beta}}}\right)$ and $\pi^{\mathrm{act}}\left(\frac{\mathrm{RANKL}}{k_{\mathrm{OC}}^{\mathrm{RANKL}}}\right)$. Indeed, these functions depend on the active and precursor cell densities. In the original models, the constants in these functions were calibrated such as to obtain a strong biochemical feedback response. Maintaining this strong biochemical response is the aim of this re-calibration.

The calibration is realised at $f_{\mathrm{bm}}=0.90$. Both the turnover rate value and the values of k_{res} and k_{form} have been changed according to the literature. Hence, by isolating $\mathrm{OB_a}$ and $\mathrm{OC_a}$ in the two new constraints of the steady state, the active osteoblast and active osteoclast read:

Table 1 Nomenclature

Symbol	Description	Value
$\overline{\chi_{BV}}$	Turnover rate	Extrapolated function of f_{bm} from Parfitt (1983)
OB_u	Uncommitted osteoblasts	Given function of f_{bm}, determined to fulfil the steady state
OC_u	Uncommitted osteoclasts	Given function of f_{bm}, determined to fulfil the steady state
k_{form}	Daily volume of bone matrix formed per osteoblast	150 μm^3/day (Buenzli et al. 2014)
k_{res}	Daily volume of bone matrix resorbed per osteoclast	9.43×10^3 μm^3/day (Buenzli et al. 2014)
λ	Strength of the mechanical transduction in formation	0.5 (parametric study)
κ	Strength of the mechanical transduction in resorption	18 pM/day (with μ_{bm}^{micro}), 19 pM/day (with μ tissue) (Parametric study)
$\mathbb{C}_{bm}^{micro}$	Stiffness tensor of the bone matrix phase	$\begin{pmatrix} 28.4 & 11.0 & 10.4 & 0 & 0 & 0 \\ 11.0 & 20.8 & 10.3 & 0 & 0 & 0 \\ 10.4 & 10.3 & 18.5 & 0 & 0 & 0 \\ 0 & 0 & 0 & 12.9 & 0 & 0 \\ 0 & 0 & 0 & 0 & 11.5 & 0 \\ 0 & 0 & 0 & 0 & 0 & 9.3 \end{pmatrix}$ GPa (Ashman et al. 1984, Fritsch and Hellmich 2007)[1]
$\mathbb{C}_{vas}^{micro}$	Stiffness tensor of the vascular phase	$2.3 \cdot \begin{pmatrix} 1 & 1 & 1 & 0 & 0 & 0 \\ 1 & 1 & 1 & 0 & 0 & 0 \\ 1 & 1 & 1 & 0 & 0 & 0 \\ 0 & 0 & 0 & 0 & 0 & 0 \\ 0 & 0 & 0 & 0 & 0 & 0 \\ 0 & 0 & 0 & 0 & 0 & 0 \end{pmatrix}$ GPa (Murdock 1996)
N_x	Normal force	−700 N (see Sect. 2.1)
M	Bending moment	50 Nm (see Sect. 2.1)
D_{OC_u}	Differentiation rate of OC_u into OC_p	0.42/day (Pivonka et al. 2013)
D_{OB_u}	Differentiation rate of OB_u into OB_p	0.7/day[2]
D_{OC_p}	Differentiation rate of OC_p into OC_a	2.1/day
D_{OB_p}	Differentiation rate of OB_p into OB_a	0.166/day
P_{OB_p}	Proliferation term of OB_p	3.5×10^{-3}/day
A_{OC_a}	Apoptosis rate of OC_a	5.65/day
A_{OB_a}	Apoptosis rate of OB_a	0.211/day
$k_{OC_a}^{TGF\beta}$	Parameter for TGFβ binding on OB_u and OC_a	5.63×10^{-4} pM
$k_{OB_p}^{TGF\beta}$	Parameter for TGFβ binding on OB_p	1.89×10^{-3} pM
k_{OB}^{PTH}	Parameter for PTH binding on OB (activator)	150 pM
k_{OB}^{PTH}	Parameter for PTH binding on OB (repressor)	0.222 pM
$k_{OC_p}^{RANKL}$	Parameter for RANKL binding on OC_p	16.65 pM
$N_{OC_p}^{RANK}$	Number of RANK receptors per OC_p	1×10^4
$k_{OC_u}^{MCSF}$	Parameter for MCSF binding on OC_u	1×10^{-3} pM (Pivonka et al. 2013)
P_{PTH}	Systemic concentration of PTH	2.907 pM
P_{PTH}^{OP}	P_{PTH} when simulated osteoporosis	2.954 pM (Parametric study)
D_{OPG}	Degradation rate of OPG	0.35/day
$\beta_{OB_a}^{OPG}$	Production rate of OPG per OB_a	1.63×10^8/day

Table 1 continued

Symbol	Description	Value
$\mathrm{OPG_{sat}}$	Saturation of OPG	2×10^8 pM
D_{RANKL}	Degradation rate of RANKL	10/day
$\beta_{\mathrm{OB_p}}^{\mathrm{RANKL}}$	Production rate of RANKL per $\mathrm{OB_p}$	1.68×10^5/day
$k_{\mathrm{OPG}}^{\mathrm{RANKL}}$	Parameter for RANKL binding on OPG	1×10^{-3}/pM
$k_{\mathrm{RANK}}^{\mathrm{RANKL}}$	Parameter for RANKL binding on RANK	0.034/pM
$D_{\mathrm{TGF\beta}}$	Degradation rate of TGFβ	2/day
$n_{\mathrm{TGF\beta}}^{\mathrm{bone}}$	Density of TGFβ stored in the bone matrix	1×10^{-2} pM
δ	Scaling parameter for the calibration of $\overline{\chi_{\mathrm{BV}}}$	0.255 (Appendix section "Recalibration of the model")
γ	Scaling parameter for the calibration of $\mathrm{OB_a}$	1.132 (Appendix section "Recalibration of the model")
β	Scaling parameter for the calibration of $\mathrm{OC_a}$	0.090 (Appendix section "Recalibration of the model")

[1]Note that in comparison with Scheiner et al. (2013), the x- and z-axes are switched.
[2]Unless otherwise specified, parameter values are taken from Buenzli et al. (2012)

$$\mathrm{OC_a^{new}} = \frac{\chi_{\mathrm{BV}}^{\mathrm{new}}}{k_{\mathrm{res}}^{\mathrm{new}}} = \beta \cdot \mathrm{OC_a} \tag{29}$$

$$\mathrm{OB_a^{new}} = \frac{k_{\mathrm{res}}^{\mathrm{new}} \cdot \mathrm{OC_a^{new}}}{k_{\mathrm{form}}^{\mathrm{new}}} = \gamma \cdot \mathrm{OB_a} \tag{30}$$

if δ is the coefficient of proportionality between the new bone turnover rate and the previous one, $\beta = \delta \cdot k_{\mathrm{res}}/k_{\mathrm{res}}^{\mathrm{new}}$ and $\gamma = \delta \cdot k_{\mathrm{form}}/k_{\mathrm{form}}^{\mathrm{new}}$. These coefficients are introduced in the determination of TGFβ and OPG. Previously, TGFβ was (Buenzli et al. 2012):

$$\mathrm{TGF\beta} = \frac{P_{\mathrm{TGF\beta}}^{\mathrm{ext}} + n_{\mathrm{TGF\beta}}^{\mathrm{bone}}\, k_{\mathrm{res}}\, \mathrm{OC_a}}{D_{\mathrm{TGF\beta}}} \tag{31}$$

The new one becomes:

$$\mathrm{TGF\beta^{new}} = \frac{P_{\mathrm{TGF\beta}}^{\mathrm{ext}} + n_{\mathrm{TGF\beta}}^{\mathrm{bone}}\, k_{\mathrm{res}}^{\mathrm{new}}\, \mathrm{OC_a^{new}} \cdot \delta^{-1}}{D_{\mathrm{TGF\beta}}} \tag{32}$$

The same manipulation is realised on the determination of OPG. The factor $\beta_{\mathrm{OB_a}}^{\mathrm{OPG}}\,\mathrm{OB_a}$ in Eq. (27) becomes $\beta_{\mathrm{OB_a}}^{\mathrm{OPG}}\,\mathrm{OB_a^{new}}\gamma^{-1}$.

Appendix 2: Update frequency of mechanical state in the numerical algorithm

In our model, to simulate osteoporosis and the change of porosity with time, we need to solve the temporal equations of the bone cell populations model, Eqs. (14)–(17) and Eq. (12). Those equations via the mechanical feedback are correlated with the spatial Eqs. (2) and (42). Knowing the porosity distribution is required to determine the stress and strain distributions. Hence, we have a semi-coupled algorithm (Fig. 2).

However, due to the separation of time scale, we can decompose the problem into two parts. Indeed, it takes more time for the microstructure to change significantly enough to influence the bone cell populations model. Therefore, we solve the bone cell populations model for a duration Δt, assuming the mechanical feedback to be constant in this time interval. Then, we recalculate the stress and strain distributions based on the new porosity distribution, and this becomes the new mechanical feedback.

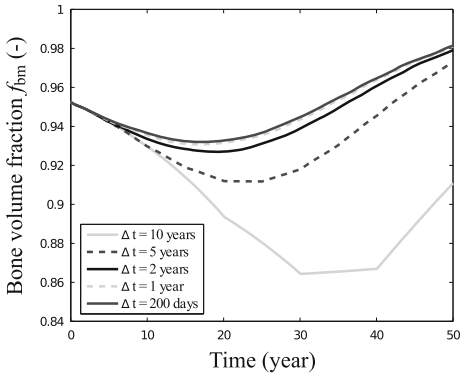

Fig. 11 The evolution of the bone matrix volume fraction for different time steps. Note that this RVE is in the intracortical region which undergoes first resorption and then formation due to the redistribution of the mechanical loads

A sensitivity analysis of the solution in the time step Δt of evolution of cell densities and bone matrix volume fraction is required. For very small time steps ($\Delta t \leq 1$ day), one would expect the algorithm to converge to the exact solution. On the other hand for very large time steps ($\Delta t \geq 5$ years), a large deviation from the exact solution is expected. Figure 11 shows the evolution of the bone matrix volume fraction for one selected RVE ($y = 0$, $z = -10$ mm) in the cross section. These simulations show that time steps of $\Delta t = 250$ days, 1 and 2 years lead to very similar evolution of the bone matrix volume fraction. On the other hand, $\Delta t = 5$ years and 10 years

lead to strong deviations from the smaller time increments. For all the simulations of 40 years of osteoporosis, we used a time step of 2 years.

Appendix 3: Generalised Beam theory for inhomogeneous materials

In the following, we represent the governing equations using a Cartesian $(x,\ y,\ z)$ coordinate system. The x-axis represents the beam axis and coincides with the direction of the vascular pores (i.e. Haversian systems). The y and z coordinates describe a material point in the cross section (Fig. 1c). The origin of the system is known as the *normal force centre*: NC. Since our cross sections are inhomogeneous all the quantities, including the stiffness, are functions of y and z.

First, based on the constitutive relation: Hooke's law, we determine the strain and stress relation:

$$\boldsymbol{\sigma}^{\text{tissue}}(y,z,t) = \mathbb{C}^{\text{tissue}}(y,z,t) : \boldsymbol{\varepsilon}^{\text{tissue}}(y,z,t) \tag{33}$$

where $\boldsymbol{\sigma}^{\text{tissue}}(y,z,t)$ and $\boldsymbol{\varepsilon}^{\text{tissue}}(y,z,t)$ are the "tissue" stress and strain and $\mathbb{C}^{\text{tissue}}(y,z,t)$ the tissue stiffness matrix. The stiffness matrix is determined at the tissue scale, and the explanation is presented in Sect. 2.1.

Based on the Bernoulli hypothesis, the strain distribution appears to be a plane and remains plane even after deformation. This is why we can decompose the strain by introducing three constants: ε_1, κ_3 and κ_2.

$$\varepsilon_{xx}^{\text{tissue}}(y,z,t) = \varepsilon_1(t) - \kappa_3(t)y + \kappa_2(t)z. \tag{34}$$

By introducing this relation into Hooke's law, we obtain:

$$\sigma_{xx}^{\text{tissue}}(y,z,t) = \mathbb{C}_{xx}^{\text{tissue}}(y,z,t)\ (\varepsilon_1(t) - \kappa_3(t)y + \kappa_2(t)z) \tag{35}$$

Because we assume the shear force to be null, the stress tensor is reduced to one component: $\sigma_{xx}^{\text{tissue}}(y,z,t)$. And with Bernoulli hypothesis, the strain tensor contains only one component. Hence, the stiffness matrix can be replaced by the component $\mathbb{C}_{xx}^{\text{tissue}}(y,z,t)$.

Here we can see that if we determine the strain constants, we would know the stress distribution. The mechanical loadings, the inputs of this model, allow us to determine the strain. Indeed, the cross section is supposed to be under a normal force: $\boldsymbol{N}$ and a bending moment $\boldsymbol{M}$ here divided in two bending moments: M_y and M_z, such as $M\ \hat{\boldsymbol{m}} = M_y\ \hat{\boldsymbol{y}} + M_z\ \hat{\boldsymbol{z}}$.

By definition of the stress, we have the relations:

$$N = \int \sigma_{xx}^{\text{tissue}}(y,z,t)\mathrm{d}A \tag{36}$$

$$M_y = \int z \cdot \sigma_{xx}^{\text{tissue}}(y,z,t)\mathrm{d}A \tag{37}$$

$$M_z = -\int y \cdot \sigma_{xx}^{\text{tissue}}(y,z,t)\mathrm{d}A \tag{38}$$

By introducing the static moments of first and second order: EA, ES_y, ES_z, EI_{yy}, EI_{zz}, EI_{yz}, the equations become the following constitutive relation:

$$\begin{bmatrix} N \\ M_y \\ M_z \end{bmatrix} = \begin{bmatrix} EA & ES_y & ES_z \\ ES_y & EI_{yy} & EI_{yz} \\ ES_z & EI_{yz} & EI_{zz} \end{bmatrix} \begin{bmatrix} \varepsilon_1 \\ \kappa_2 \\ \kappa_3 \end{bmatrix} \tag{39}$$

where:

$$EA = \int \mathbb{C}_{xx}^{\text{tissue}}(y,z,t)\mathrm{d}A$$

$$ES_y = \int \mathbb{C}_{xx}^{\text{tissue}}(y,z,t) \cdot y\mathrm{d}A$$

$$EI_{yy} = \int \mathbb{C}_{xx}^{\text{tissue}}(y,z,t) \cdot y^2\mathrm{d}A$$

$$ES_z = \int \mathbb{C}_{xx}^{\text{tissue}}(y,z,t) \cdot z\mathrm{d}A$$

$$EI_{zy} = \int \mathbb{C}_{xx}^{\text{tissue}}(y,z,t) \cdot yz\mathrm{d}A = EI_{yz}$$

$$EI_{zz} = \int \mathbb{C}_{xx}^{\text{tissue}}(y,z,t) \cdot z^2\mathrm{d}A$$

If we chose the origin of the coordinate system at the normal centre (NC) of the cross section, the coupling terms between extension and bending vanish since they become null by definition of the NC:

$$ES_y = \int \mathbb{C}_{xx}^{\text{tissue}}(y,z,t) \cdot y\mathrm{d}A = 0 \tag{40}$$

$$ES_z = \int \mathbb{C}_{xx}^{\text{tissue}}(y,z,t) \cdot z\mathrm{d}A = 0 \tag{41}$$

The constitutive relation can be simplified as:

$$\begin{bmatrix} N \\ M_y \\ M_z \end{bmatrix} = \begin{bmatrix} EA & 0 & 0 \\ 0 & EI_{yy} & EI_{yz} \\ 0 & EI_{yz} & EI_{zz} \end{bmatrix} \begin{bmatrix} \varepsilon_1 \\ \kappa_2 \\ \kappa_3 \end{bmatrix} \tag{42}$$

Determination of the normal force centre NC

The special location of the origin of the coordinate system for which the coupling terms (ES_y and ES_z) between extension and bending become zero is by definition called the normal force centre NC. The result of this definition is that

an axial force N which acts at the NC only causes straining and no bending. The coupling terms are also referred to as weighted static moments or weighted first order moments. To find the position of the coordinate system for which the coupling terms become zero requires a tool.

Assume a temporary coordinate system: $\overline{y}-\overline{z}$ from which the porosity distribution is known. The shift in origin of this coordinate system with respect to the y–z coordinate system through the unknown NC is denoted with $\overline{y}_{NC}$ and $\overline{z}_{NC}$. The temporary coordinate system can be expressed in terms of the y–z coordinate system as:

$$\overline{y} = y + \overline{y}_{NC} \qquad \overline{z} = z + \overline{z}_{NC}$$

Hence:

$$\begin{aligned} ES_{\overline{y}} &= \int \mathbb{C}_{xx}^{\text{tissue}}(y,z,t)\cdot \overline{y}\,\mathrm{d}A \\ &= \int \mathbb{C}_{xx}^{\text{tissue}}(y,z,t)\cdot y\,\mathrm{d}A + \overline{y}_{NC}\int \mathbb{C}_{xx}^{\text{tissue}}(y,z,t)\mathrm{d}A \\ &= ES_y + EA\cdot \overline{y}_{NC} \end{aligned} \tag{43}$$

$$\begin{aligned} ES_{\overline{z}} &= \int \mathbb{C}_{xx}^{\text{tissue}}(y,z,t)\cdot \overline{z}\,\mathrm{d}A \\ &= \int \mathbb{C}_{xx}^{\text{tissue}}(y,z,t)\cdot z\,\mathrm{d}A + \overline{z}_{NC}\int \mathbb{C}_{xx}^{\text{tissue}}(y,z,t)\mathrm{d}A \\ &= ES_z + EA\cdot \overline{z}_{NC} \end{aligned} \tag{44}$$

By definition, ES_y and ES_z with respect to the y–z coordinate system are zero from which the unknown position of the NC with respect to the known position of the $\overline{y}$–$\overline{z}$ coordinate system can be found:

$$\overline{y}_{NC} = \frac{ES_{\overline{y}}}{EA} \tag{45}$$

$$\overline{z}_{NC} = \frac{ES_{\overline{z}}}{EA} \tag{46}$$

To conclude, here is the step-by-step methodology we are using to find the stress and strain distribution in the cross section:

1. Localise the normal centre (NC) by computing the integrations: EA, ES_y, ES_z.
2. Compute the integrations: EI_{yy}, EI_{zz} and EI_{yz}.
3. Determine the cross-sectional forces: N, M_y and M_z.
4. Calculate the cross-sectional deformations: ε_1, κ_2 and κ_3 based on Eq. (42).
5. Find the strain distribution based on the kinematic relation, Eq. (34). Here it is important to remember to use the coordinate centred in NC.
6. Find the stress distribution based on Hooke's law, Eq. (33).

The initial cross section is extracted from a microradiograph, as it is explained in Sect. 2.4; the mechanical loading is not symmetrical. Hence, the position of the NC is changing. This is why we need to localise it after each step.

References

Adachi T, Aonuma Y, Ito SI, Tanaka M, Hojo M, Takano-Yamamoto T, Kamioka H (2009a) Osteocyte calcium signaling response to bone matrix deformation. J Biomech 42(15):2507–2512

Adachi T, Aonuma Y, Tanaka M, Hojo M, Takano-Yamamoto T, Kamioka H (2009) Calcium response in single osteocytes to locally applied mechanical stimulus: Differences in cell process and cell body. J Biomech 42(12):1989–1995. doi:10.1016/j.jbiomech.2009.04.034

Ashman R, Cowin S, Van Buskirk W, Rice J (1984) A continuous wave technique for the measurement of the elastic properties of cortical bone. J Biomech 17(5):349–361. doi:10.1016/0021-9290(84)90029-0

Ausk BJ, Huber P, Poliachik SL, Bain SD, Srinivasan S, Gross TS (2012) Cortical bone resorption following muscle paralysis is spatially heterogeneous. Bone 50(1):14–22

Ausk BJ, Huber P, Srinivasan S, Bain SD, Kwon RY, McNamara EA, Poliachik SL, Sybrowsky CL, Gross TS (2013) Metaphyseal and diaphyseal bone loss in the tibia following transient muscle paralysis are spatiotemporally distinct resorption events. Bone 57(2):413–422

Bauchau OA, Craig JI (2009) Structural analysis. With applications to aerospace structures, solid mech edn. Springer, Berlin

Bloomfield SA, Allen MR, Hogan HA, Delp MD (2002) Site- and compartment-specific changes in bone with hindlimb unloading in mature adult rats. Bone 31(1):149–157

Bonewald LF (2011) The amazing osteocyte. J Bone Miner Res 26(2):229–38

Bonewald LF, Johnson ML (2008) Osteocytes, mechanosensing and Wnt signaling. Bone 42(4):606–15

Bousson V, Meunier A, Bergot C, Vicaut E, Rocha MA, Morais MH, Laval-Jeantet AM, Laredo JD (2001) Distribution of intracortical porosity in human midfemoral cortex by age and gender. J Bone Miner Res 16(7):1308–17. doi:10.1359/jbmr.2001.16.7.1308

Buenzli PR, Sims NA (2015) Quantifying the osteocyte network in the human skeleton. Bone (In Press), doi:10.1016/j.bone.2015.02.016

Buenzli PR, Pivonka P, Gardiner BS, Smith DW (2012) Modelling the anabolic response of bone using a cell population model. J Theor Biol 307:42–52

Buenzli PR, Thomas CDL, Clement JG, Pivonka P (2013) Endocortical bone loss in osteoporosis: the role of bone surface availability. Int J Numer Methods Biomed Eng 29(12):1307–1322. doi:10.1002/cnm.2567

Buenzli PR, Pivonka P, Smith DW (2014) Bone refilling in cortical basic multicellular units: insights into tetracycline double labelling from a computational model. Biomech Model Mechanobiol 13(1):185–203. doi:10.1007/s10237-013-0495-y

Burger EH, J Klein-Nulend, Jand Smit TH (2003) Strain-derived canalicular fluid flow regulates osteoclast activity in a remodelling osteon: a proposal. J Biomech 36:1453–1459. doi:10.1016/S0021-9290(03)00126-X

Burghardt AJ, Kazakia GJ, Sode M, de Papp AE, Link TM, Majumdar S (2010) A longitudinal HR-pQCT study of alendronate treatment in postmenopausal women with low bone density: Relations among density, cortical and trabecular microarchitecture, biomechanics, and bone turnover. J Bone Miner Res 25(12):2558–2571

Burr D (1997) Muscle strength, bone mass, and age related bone loss. J Bone Miner Res 12(10):1547–1551. doi:10.1359/jbmr.1997.12.10.1547

Burr DB, Hirano T, Turner CH, Hotchkiss C, Brommage R, Hock JM (2001) Intermittently administered human parathyroid hormone(1–34) treatment increases intracortical bone turnover and porosity without reducing bone strength in the humerus of ovariectomized cynomolgus monkeys. J Bone Miner Res 16(1):157–165. doi:10.1359/jbmr.2001.16.1.157

Busse B, Bale HA, Zimmermann EA, Panganiban B, Barth HD, Carriero A, Vettorazzi E, Zustin J, Hahn M, Ager JW, Püschel K, Amling M, Ritchie RO (2013) Vitamin D deficiency induces early signs of aging in human bone, increasing the risk of fracture. Sci Transl Med 5(193):1–11. doi:10.1126/scitranslmed.3006286

Carpenter RD, Carter DR (2008) The mechanobiological effects of periosteal surface loads. Biomech Model Mechanobiol 7(3):227–242. doi:10.1007/s10237-007-0087-9

Carter DR, Beaupré GS (2001) Skeletal function and form. Cambridge University Press, Cambridge

Carter DR, Hayes WC (1977) The compressive behavior porous of bone structure as a two-phase. J Bone Joint Surg 59(7):954–962

Chappard D, Retailleau-Gaborit N, Legrand E, Baslé MF, Audran M (2005) Comparison insight bone measurements by histomorphometry and microCT. J Bone Miner Res 20(7):1177–1184

Christen P, Ito K, Müller R, Rubin MR, Dempster DW, Bilezikian JP, Van Rietbergen B (2012) Patient-specific bone modelling and remodelling simulation of hypoparathyroidism based on human iliac crest biopsies. J Biomech 45(14):2411–2416

Christen P, Ito K, Santos AAD, Müller R, van Rietbergen B (2013) Validation of a bone loading estimation algorithm for patient-specific bone remodelling simulations. J Biomech 46(5):941–948

Collet P, Uebelhart D, Vico L, Moro L, Hartmann D, Roth M, Alexandre C (1997) Effects of 1- and 6-month spaceflight on bone mass and biochemistry in two humans. Bone 20(6):547–551

Cordey J, Gautier E (1999) Strain gauges used in the mechanical testing of bones. Part III: strain analysis, graphic determination of the neutral axis. Injury 30:SA21–SA25

Dempster DW, Compston JE, Drezner MK, Glorieux FH, Kanis JA, Malluche H, Meunier PJ, Ott SM, Recker RR, Parfitt AM (2013) Standardized nomenclature, symbols, and units for bone histomorphometry: a 2012 update of the report of the ASBMR histomorphometry nomenclature committee. J Bone Miner Res 28(1):2–17. doi:10.1002/jbmr.1805

Eser P, Frotzler A, Zehnder Y, Wick L, Knecht H, Denoth J, Schiessl H (2004) Relationship between the duration of paralysis and bone structure: a pQCT study of spinal cord injured individuals. Bone 34:869–880

Eshelby JD (1957) The determination of the elastic field of an ellipsoidal inclusion, and related problems. Proc R Soc A Math Phys Eng Sci 241(1226):376–396

Fan X, Roy E, Zhu L, Murphy TC, Ackert-Bicknell C, Hart CM, Rosen C, Nanes MS, Rubin J (2004) Nitric oxide regulates receptor activator of nuclear factor-kappaB ligand and osteoprotegerin expression in bone marrow stromal cells. Endocrinology 145(2):751–759. doi:10.1210/en.2003-0726

Feik SA, Thomas CD, Clement JG (1997) Age-related changes in cortical porosity of the midshaft of the human femur. J Anat 191:407–416

Feik SA, Thomas CD, Bruns R, Clement JG (2000) Regional variations in cortical modeling in the femoral mid-shaft: sex and age differences. Am J Phys Anthropol 112(2):191–205

Felsenberg D, Boonen S (2005) The bone quality framework: determinants of bone strength and their interrelationships, and implications for osteoporosis management. Clin Ther 27(1):1–11

Forner-Cordero A, Koopman HJFM, Van der Helm FCT (2006) Inverse dynamics calculations during gait with restricted ground reaction force information from pressure insoles. Gait Posture 23(2):189–199

Fritsch A, Hellmich C, Dormieux L (2009) Ductile sliding between mineral crystals followed by rupture of collagen crosslinks: experimentally supported micromechanical explanation of bone strength. J Theor Biol 260(2):230–252. doi:10.1016/j.jtbi.2009.05.021

Fritsch A, Hellmich C (2007) 'Universal' microstructural patterns in cortical and trabecular, extracellular and extravascular bone materials: micromechanics-based prediction of anisotropic elasticity. J Theor Biol 244(4):597–620. doi:10.1016/j.jtbi.2006.09.013

Frost HM (1987) Bone "mass" and the "mechanostat": a proposal. Anat Rec 219(1):1–9. doi:10.1002/ar.1092190104

Frost HM (1997) On our age-related bone loss: insights from a new paradigm. J Bone Miner Res 12(10):1539–1546. doi:10.1359/jbmr.1997.12.10.1539

Frost HM (2003) Bone's mechanostat: a 2003 update. Anat Rec A Discov Mol Cell Evol Biol 275(2):1081–1101. doi:10.1002/ar.a.10119

Fyhrie DP, Carter DR (1986) A unifying principle relating stress to trabecular bone morphology. J Orthop Res 4(3):304–317

Fyhrie DP, Kimura JH (1999) Cancellous bone biomechanics. J Biomech 32(11):1139–1148. doi:10.1016/S0021-9290(99)00114-1

García-Aznar JM, Rueberg T, Doblare M (2005) A bone remodelling model coupling micro-damage growth and repair by 3D BMU-activity. Biomech Model Mechanobiol 4(2–3):147–167. doi:10.1007/s10237-005-0067-x

Gitman IM, Askes H, Kuhl E, Aifantis EC (2010) Stress concentrations in fractured compact bone simulated with a special class of anisotropic gradient elasticity. Int J Solids Struct 47(9):1099–1107. doi:10.1016/j.ijsolstr.2009.11.020

Hellmich C, Ulm FJ, Dormieux L (2004) Can the diverse elastic properties of trabecular and cortical bone be attributed to only a few tissue-independent phase properties and their interactions? Arguments from a multiscale approach. Biomech Model Mechanobiol 2(4):219–238. doi:10.1007/s10237-004-0040-0

Hellmich C, Kober C, Erdmann B (2008) Micromechanics-based conversion of CT data into anisotropic elasticity tensors, applied to FE simulations of a mandible. Ann Biomed Eng 36(1):108–122. doi:10.1007/s10439-007-9393-8

Hernandez CJ, Beaupré GS, Keller TS, Carter DR (2001) The influence of bone volume fraction and ash fraction on bone strength and modulus. Bone 29(1):74–78

Hill R (1963) Elastic properties of reinforced solids. J Mech Phys Solids 11(5):357–372

Hill R (1965) A self-consistent mechanics of composite materials. J Mech Phys Solids 13(4):213–222. doi:10.1016/0022-5096(65)90010-4

Hipp JA, Edgerton BC, An KN, Hayes WC (1990) Structural consequences of transcortical holes in long bones loaded in torsion. J Biomech 23:1261–1268

Hirano T, Burr DB, Cain RL, Hock JM (2000) Changes in geometry and cortical porosity in adult, ovary-intact rabbits after 5 months treatment with LY333334 (hPTH 1–34). Calcif Tissue Int 66:456–460. doi:10.1007/s002230010091

Hjelmstad KD (2005) Fundamentals of structural mechanics, 2nd edn. Springer, Berlin

Huiskes R, Ruimerman R, Van Lenthe GH, Janssen JD (2000) Effects of mechanical forces on maintenance and adaptation of form in trabecular bone. Nature 405(6787):704–706. doi:10.1038/35015116

Jepsen KJ, Andarawis-Puri N (2012) The amount of periosteal apposition required to maintain bone strength during aging depends on adult bone morphology and tissue-modulus degradation rate. J Bone Miner Res 27(9):1916–1926. doi:10.1002/jbmr.1643

Jones SH (1974) Secretory territories and rates of matrix production of osteoblasts. Calcif Tissue Res 14:309–315

Judex S, Garman R, Squire M, Busa B, Donahue LR, Rubin C (2004) Genetically linked site-specificity of disuse osteoporosis. J Bone Miner Res 19(4):607–613. doi:10.1359/JBMR.040110

Kasiri S, Taylor D (2008) A critical distance study of stress concentrations in bone. J Biomech 41:603–609. doi:10.1016/j.jbiomech.2007.10.003

Kaspar D, Seidl W, Neidlinger-Wilke C, Beck A, Claes L, Ignatius A (2002) Proliferation of human-derived osteoblast-like cells depends on the cycle number and frequency of uniaxial strain. J Biomech 35(7):873–880. doi:10.1016/S0021-9290(02)00058-1

Kerschnitzki M, Kollmannsberger P, Burghammer M, Duda GN, Weinkamer R, Wagermaier W, Fratzl P (2013) Architecture of the osteocyte network correlates with bone material quality. J Bone Miner Res 28(8):1837–1845. doi:10.1002/jbmr.1927

Kiratli BJ, Smith AE, Nauenberg T, Kallfelz CF, Perkash I (2000) Bone mineral and geometric changes through the femur with immobilization due to spinal cord injury. J Rehabil Res Dev 37:225–233

Knothe Tate ML, Knothe U, Niederer P (1998) Experimental elucidation of mechanical load-induced fluid flow and its potential role in bone metabolism and functional adaptation. Am J Med Sci 316(3):189–195

Knothe Tate ML (2003) Whither flows the fluid in bone? An osteocyte's perspective. J Biomech 36(10):1409–1424. doi:10.1016/S0021-9290(03)00123-4

Lang T, LeBlanc A, Evans H, Lu Y, Genant H, Yu A (2004) Cortical and trabecular bone mineral loss from the spine and hip in long-duration spaceflight. J Bone Miner Res 19(6):1006–1012

Lanyon LE, Goodship AE, Pye CJ, MacFie JH (1982) Mechanically adaptive bone remodelling. J Biomech 15(3):141–154

Lanyon LE, Rubin CT (1984) Static versus dynamic loads as an influence on bone remodelling. J Biomech 17(12):897–905

Laws N (1977) The determination of stress and strain concentrations at an ellipsoidal inclusion in an anisotropic material. J Elast 7(1):91–97

Leblanc AD, Spector ER, Evans HJ, Sibonga JD (2007) Skeletal responses to space flight and the bed rest analog: a review. J Musculoskelet Neuronal Interact 7(1):33–47

Lemaire V, Tobin FL, Greller LD, Cho CR, Suva LJ (2004) Modeling the interactions between osteoblast and osteoclast activities in bone remodeling. J Theor Biol 229(3):293–309. doi:10.1016/j.jtbi.2004.03.023

Lerebours C, Thomas C, Clement J, Buenzli P, Pivonka P (2015) The relationship between porosity and specific surface in human cortical bone is subject specific. Bone 72:109–117. doi:10.1016/j.bone.2014.11.016

Levenston ME, Carter DR (1998) An energy dissipation-based model for damage stimulated bone adaptation. J Biomech 31(7):579–586

Lloyd DG, Besier TF (2003) An EMG-driven musculoskeletal model to estimate muscle forces and knee joint moments in vivo. J Biomech 36(6):765–776. doi:10.1016/S0021-9290(03)00010-1

Malluche HH, Porter DS, Monier-Faugere M, Mawad H, Pienkowski D (2012) Differences in bone quality in low- and high-turnover renal osteodystrophy. J Am Soc Nephrol 23(3):525–532. doi:10.1681/ASN.2010121253

Marotti G (2000) The osteocyte as a wiring transmission system. J Musculoskelet Neuronal Interact 1(2):133–136

Marotti G, Zallone AZ (1976) Number, size and arrangement of osteoblasts in osteons at different stages of formation. Calcif Tissue Int 21(suppl):96

Martelli S, Pivonka P, Ebeling PR (2014) Femoral shaft strains during daily activities: implications for atypical femoral fractures. Clin Biomech 29(8):869–876. doi:10.1016/j.clinbiomech.2014.08.001

Martin RB (1972) Effects of geometric feedback in osteoporosis. J Biomech 5:447–455

Martin RB (1984) Porosity and specific surface of bone. Crit Rev Biomed Eng 10(3):179–222

Martin TJ (2004) Paracrine regulation of osteoclast formation and activity: milestones in discovery. J Musculoskelet Neuronal Interact 4(3):243–253

McNamara LM, Prendergast PJ (2007) Bone remodelling algorithms incorporating both strain and microdamage stimuli. J Biomech 40(6):1381–1391

Mittlmeier T, Mattheck C, Dietrich F (1994) Effects of mechanical loading on the profile of human femoral diaphyseal geometry. Med Eng Phys 16:75–81. doi:10.1016/1350-4533(94)90014-0

Morin C, Hellmich C (2014) A multiscale poromicromechanical approach to wave propagation and attenuation in bone. Ultrasonics 54(5):1251–1269. doi:10.1016/j.ultras.2013.12.005

Mosekilde L (1990) Consequences of the remodeling process for vertebral trabecular bone-structure: a scanning electron-microscopy study (uncoupling of unloaded structures). Bone Miner 10:13–35

Mullender MG, Huiskes R, Weinans H (1994) A physiological approach to the simulation of bone remodeling as a self-organizational control process. J Biomech 27(11):1389–1394

Murdock J (1996) Mechanics of Fluids. In: McGraw-Hill (ed) Mark's standard handbook for mechanical engineers, 10th edn, McGraw-Hill, pp 3.29–3.61

Nordin BEC, Need AG, Chatterton BE, Horowitz M, Morris HA (1988) The relative contributions of age and years since menopause to postmenopausal bone loss. J Clin Endocrinol Metab 70(1):83–88

Parfitt A (1983) The physiologic and clinical significance of bone histomorphometric data. In: Recker R (ed) Bone histomorphometry: techniques and interpretation, chap 9. CRC Press, Boca Raton, pp 143–224

Parfitt AM, Drezner MK, Glorieux FH, Kanis JA, Malluche H, Meunier PJ, Ott SM, Recker RR (1987) Bone histomorphometry: standardization of nomenclature, symbols, and units. Report of the ASBMR histomorphometry nomenclature committee. J Bone Miner Res 2(6):595–610. doi:10.1002/jbmr.5650020617

Parfitt A (1998) A structural approach to renal bone disease. J Bone Miner Res 13(8):1213–1220

Parfitt A, Chir B (1987) Bone remodeling and bone loss: understanding the pathophysiology of osteoporosis. Clin Obstet Gynecol 30(4):789–811

Pettermann H, Reiter T, Rammerstorfer F (1997) Computational simulation of internal bone remodeling. Archiv Comput Methods Eng 4(4):295–323

Pivonka P, Zimak J, Smith DW, Gardiner BS, Dunstan CR, Sims NA, Martin TJ, Mundy GR (2008) Model structure and control of bone remodeling: a theoretical study. Bone 43(2):249–263. doi:10.1016/j.bone.2008.03.025

Pivonka P, Zimak J, Smith DW, Gardiner BS, Dunstan CR, Na Sims, Martin TJ, Mundy GR (2010) Theoretical investigation of the role of the RANK–RANKL–OPG system in bone remodeling. J Theor Biol 262(2):306–316. doi:10.1016/j.jtbi.2009.09.021

Pivonka P, Buenzli PR, Scheiner S, Hellmich C, Dunstan CR (2013) The influence of bone surface availability in bone remodelling: a mathematical model including coupled geometrical and biomechanical regulations of bone cells. Eng Struct 47:134–147

Pivonka P, Buenzli PR, Dunstan CR (2012) A systems approach to understanding bone cell interactions in health and disease. In: Gowder S (ed) Cell interactions, chap. 7

Prendergast PJ, Taylor D (1994) Prediction of bone adaptation using damage accumulation. J Biomech 27(8):1067–1076

Raisz LG, Seeman E (2001) Causes of age-related bone loss and bone fragility: an alternative view. J Bone Miner Res 16(11):1948–1952

Rho JY, Kuhn-Spearing L, Zioupos P (1998) Mechanical properties and the hierarchical structure of bone. Med Eng Phys 20(2):92–102

Rittweger J, Simunic B, Bilancio G, Gaspare De Santo N, Cirillo M, Biolo G, Pisot R, Eiken O, Mekjavic IB, Narici M (2009) Bone

loss in the lower leg during 35 days of bed rest is predominantly from the cortical compartment. Bone 44(4):612–618. doi:10.1016/j.bone.2009.01.001

Robling AG, Castillo AB, Turner CH (2006) Biomechanical and molecular regulation of bone remodeling. Annu Rev Biomed Eng 8:455–498

Roodman GD (1999) Cell biology of the osteoclast. Exp Hematol 27(8):1229–1241

Ruff CB (2000) Body size, body shape, and long bone strength in modern humans. J Hum Evol 38(2):269–290. doi:10.1006/jhev.1999.0322

Ruimerman R, Van Rietbergen B, Hilbers P, Huiskes R (2005) The effects of trabecular-bone loading variables on the surface signaling potential for bone remodeling and adaptation. Ann Biomed Eng 33(1):71–78

Russo CR, Lauretani F, Seeman E, Bartali B, Bandinelli S, Di Iorio A, Guralnik J, Ferrucci L (2006) Structural adaptations to bone loss in aging men and women. Bone 38:112–118. doi:10.1016/j.bone.2005.07.025

Salencon J (2001) Handbook of continuum mechanics (general concepts, thermoelasticity), 1st edn. Springer, Berlin

Scheiner S, Pivonka P, Hellmich C (2013) Coupling systems biology with multiscale mechanics, for computer simulations of bone remodeling. Comput Methods Appl Mech Eng 254:181–196. doi:10.1016/j.cma.2012.10.015

Skerry TM, Bitensky L, Chayen J, Lanyon LE (1988) Loading-related reorientation of bone proteoglycan in vivo. Strain memory in bone tissue? J Orthop Res 6(4):547–551

Squire M, Brazin A, Keng Y, Judex S (2008) Baseline bone morphometry and cellular activity modulate the degree of bone loss in the appendicular skeleton during disuse. Bone 42(2):341–349. doi:10.1016/j.bone.2007.09.052

Szulc P, Seeman E, Duboeuf F, Sornay-Rendu E, Delmas PD (2006) Bone fragility: failure of periosteal apposition to compensate for increased endocortical resorption in postmenopausal women. J Bone Miner Res 21(12):1856–1863. doi:10.1359/jbmr.060904

Tan SD, de Vries TJ, Kuijpers-Jagtman AM, Semeins CM, Everts V, Klein-Nulend J (2007) Osteocytes subjected to fluid flow inhibit osteoclast formation and bone resorption. Bone 41:745–751. doi:10.1016/j.bone.2007.07.019

Thomas CDL, Feik SA, Clement JG (2005) Regional variation of intracortical porosity in the midshaft of the human femur: age and sex differences. J Anat 206(2):115–125. doi:10.1111/j.1469-7580.2005.00384.x

Timoshenko S, Goodier JN (1951) Theory of elasticity. McGraw-Hill, New York

Turner CH, Robling AG, Duncan RL, Burr DB (2002) Do bone cells behave like a neuronal network? Calcif Tissue Int 70(6):435–442

Van der Meulen MCH, Beaupre GS, Carter DR (1993) Mechanobiologic influences in long bone cross-sectional growth. Bone 14(4):635–642

Van Oers RFM, Ruimerman R, Tanck E, Hilbers PAJ, Huiskes R (2008) A unified theory for osteonal and hemi-osteonal remodeling. Bone 42(2):9–250. doi:10.1016/j.bone.2007.10.009

Van Rietbergen B, Müller R, Ulrich D, Rüegsegger P, Huiskes R (1999) Tissue stresses and strain in trabeculae of a canine proximal femur can be quantified from computer reconstructions. J Biomech 32(4):51–443

Vaughan CL, Davis BL, O'Connor JC (1992) Dynamics of human gait. Kiboho Publishers, Cape Town

Viceconti M, Testi D, Taddei F, Martelli S, Clapworthy GJ, Jan S (2006) Biomechanics modeling of the musculoskeletal apparatus : status and key issues. Proc IEEE 94(4):725–739

Vico L, Collet P, Guignandon A, Lafage-Proust MH, Thomas T, Rehailia M, Alexandre C (2000) Effects of long-term microgravity exposure on cancellous and cortical weight-bearing bones of cosmonauts. Lancet 355(9215):1607–1611. doi:10.1016/S0140-6736(00)02217-0

Wang FS, Wang CJ, Chen YJ, Huang YT, Huang HC, Chang PR, Sun YC, Yang KD (2004) Nitric oxide donor increases osteoprotegerin production and osteoclastogenesis inhibitory activity in bone marrow stromal cells from ovariectomized rats. Endocrinology 145:2148–2156

Warner SE, Sanford DA, Becker BA, Bain SD, Srinivasan S, Gross TS (2006) Botox induced muscle paralysis rapidly degrades bone. Bone 38:257–264

Weinans H, Huiskes R, Grootenboer HJ (1992) The behavior of adaptive bone-remodeling simulation models. J Biomech 25(12):1425–1441

Weinbaum S, Cowin S, Zeng Y (1994) A model for the excitation of osteocytes by mechanical loading-induced bone fluid shear stresses. J Biomech 27(3):339–360. doi:10.1016/0021-9290(94)90010-8

Weiner S, Wagner HD (1998) The material bone: structure-mechanical function relations. Annu Rev Mater Sci 28(1):271–298

Weyts F, Bosmans B, Niesing R, Van Leeuwen J, Weinans H (2003) Mechanical control of human osteoblast apoptosis and proliferation in relation to differentiation. Calcif Tissue Int 72(4):505–512. doi:10.1007/s00223-002-2027-0

Zaoui A (1997) Structural morphology and constitutive behavior of microheterogeneous materials. In: Suquet P (ed) Continuum Micromech. Springer, Wien, pp 291–347

Zaoui A (2002) Continuum micromechanics: survey. J Eng Mech 128(August):808–816

Zebaze RMD, Ghasem-Zadeh A, Bohte A, Iuliano-Burns S, Mirams M, Price RI, Mackie EJ, Seeman E (2010) Intracortical remodelling and porosity in the distal radius and post-mortem femurs of women: a cross-sectional study. Lancet 375(9727):1729–1736. doi:10.1016/S0140-6736(10)60320-0